Wear-resistant CrCoNi nanocrystalline film via friction-driven surface segregation

Qing Zhou [a,b], Zhichao Jiao [a], Zhuobin Huang [a], Yeran Shi [a], Yulong Li [b], Cunhong Yin [c], Haifeng Wang [a,*], Haroldo Cavalcanti Pinto [b,d], Christian Greiner [b,*], Weimin Liu [a,e]

[a] Center of Advanced Lubrication and Seal Materials, Research & Development Institute of Northwestern Polytechnical University in Shenzhen, Guang Dong, 518063, China
[b] Institute for Applied Materials (IAM), Karlsruhe Institute of Technology (KIT), Kaiserstr. 12, 76131 Karlsruhe, Germany
[c] College of Mechanical Engineering, Guizhou University, Guiyang Guizhou, 550025, China
[d] São Carlos School of Engineering-EESC, University of São Paulo-USP, São Carlos 13563-120, Brazil
[e] State Key Laboratory of Solid Lubrication, Lanzhou Institute of Chemical Physics, Chinese Academy of Sciences, Lanzhou, 730000, China

ABSTRACT

Revealing the frictional behavior through the lens of structural and chemical evolution is crucial for comprehending the exceptional wear-resistance of alloys with complex composition. Here, we propose that superior wear resistance can be achieved via dynamic surface segregation during sliding at room temperature. This strategy was demonstrated in CrCoNi multi-principal element alloy (MPEA) films with nano-grain structure, which exhibit a remarkably low wear rate that is <50 % of that for their VCoNi counterpart. Such distinct wear behavior is attributed to the specific friction-driven Ni segregation on the CrCoNi surface, which facilitates the preferential oxidation and formation of a nanocomposite protective layer with equiaxed nanograins uniformly embedded in an amorphous matrix. This wear-induced unique microstructure accommodates sliding-induced plastic deformation against damage and is responsible for the superior wear-resistance. Having revealed these fundamental mechanisms by experiment and simulation, this study provides a brand-new perception for designing self-adaptive MPEA surfaces. This involves adjusting the evolution of deformation layers with specific structure and chemistry, precisely engineered for tribological applications.

1. Introduction

During most mechanical operations, friction and wear exert a significant impact on work efficiency, reliability and service life [1,2]. Sliding friction of alloys will lead to the removal of surface material, associated with the evolution of subsurface microstructure, compositional change, cracking initiation and propagation [3,4]. The microstructure of subsurface layer tends to diverge from the undeformed substrate in terms of structure and component, potentially undergoing grain refinement [5], grain boundary relaxation [6], dynamic recrystallization [7], frictional oxidation [8] and self-organized protective layer [9]. These changes can significantly influence tribological behavior. Thus, revealing the microstructural and chemical of worn surfaces is of guiding significance for understanding the wear behavior, which is conducive to the effective design of advanced alloys and films.

In recent years, the proposal of multi-principal element alloys (MPEAs), composed of multiple main components, has subverted the conventions of alloy design with a single component and attracted widespread attention [10-12]. Most MPEAs exhibit superior mechanical properties due to their unique effect of lattice distortion. These properties provide broad possibilities for breaking through the wear-resistant limitations of traditional alloys [13-16]. Grain refinement is one of the common approaches for strengthening and enhancing wear-resistance of MPEAs [17]. Reports indicate that nanostructured MPEA films can be grown by magnetron sputtering, inheriting the excellent functional properties of bulk MPEAs while enhancing their superior mechanical characteristics [18]. For example, the as-deposited NbMoWTa MPEA with an average grain size of ~70 nm presents a yield strength of ~8 GPa, nearly six times stronger than bulk MPEA of the same composition [19]. However, due to the brittle nature of nanograins, the cyclic stress during friction will lead to strain localization, cracking and film delamination, which is detrimental to the wear performance [20,21].

Despite its limited ductility, the spontaneous formation of gradient structures and oxide protective layers under specific service conditions enhances wear-resistance [22-24]. For instance, Luo et al. [22] reported on the presence of self-organized gradient nanostructures induced by sliding wear at 300 ℃. This facilitates plastic co-deformation and suppressed strain localization, effectively enhancing the tribological performance with reduced COF and wear loss. Similarly, Liang et al. [23] demonstrated that a strong and ductile heterogeneous glaze layer with a thickness of 3 μm, composed of nanograined oxide and ultrafine grained matrix, achieved hetero-deformation induced strengthening with a great capacity to accommodate tribological strain. Besides, it is established that MPEAs featuring an amorphous-crystalline nanocomposite structure can surmount the strength-ductility compromise typically verified in mono-phase materials, thereby delivering exceptional mechanical properties with near-theoretical strength [25]. Inspired by this strategy, the amorphous-crystalline nanocomposite has been introduced into worn surface, thus help improving the wear-resistance. For example, Liu et al. [26] illustrated that an oxide nanocomposite surface with Ag nanoparticles embedded in TiZrNbO amorphous matrix, formed by the reactive wear with environments, achieves a satisfactory combination of strength, toughness and wear resistance.

In addition to mechanical consideration, the surface of MPEAs has been observed to undergo element redistribution as a result of oxidation or sliding at elevated temperatures, leading to the formation of a protective layer that effectively reduces wear. Specifically, a manganese-rich oxide layer was identified on the surface of CoCrFeNiMn through static oxidation at 1150 ℃, serving to impede oxygen erosion [27]. Yang et al. [28] attributed the noticeable improvement in wear-resistance to element redistribution forming two distinct sublayers during sliding tests at 600 ℃. However, the occurrence of element redistribution typically requires high temperatures and is rare to be observed at room temperature, thus hampering its utilization to improve the wear-resistance of alloys at ambient service conditions. These challenges when thoroughly investigated would help guide MPEA's transition from being just complex alloys with simple-solid solution structures to industrially applicable high-performance alloys.

In this work, we demonstrate that the worn surface with a desirable structure for wear protection can be tuned via surface segregation upon sliding even at room temperature. This strategy was successfully implemented in a CrCoNi ternary MPEA film with nano-grain structure, where atomic characteristics dependent surface segregation and deformed microstructure during sliding were captured through both experiment and simulation. This friction-driven element segregation, however, did not take place in a VCoNi ternary MPEA film with a similar microstructure. In contrast, selective oxidation and formation of the protective layer with amorphous-crystalline nanocomposite structure can be verified on the CrCoNi surface. This unique microstructure facilitates homogeneous sliding-induced plastic deformation, significantly enhancing wear-resistance of CrCoNi compared to VCoNi. The present work then provides a brand-new perspective on designing self-adaptive MPEA film with excellent wear-resistance for tribological applications.

2. Experimental and simulation methods

2.1. Sample preparation

In order to clarify the effect of composition on surface chemical/structural evolution, two representative and structurally similar ternary MPEAs, i.e., CrCoNi and VCoNi [29], were chosen as the subjects. The MPEA films were prepared by magnetron-sputtering at room temperature, using CrCoNi and VCoNi targets with equiatomic composition, respectively. The samples were deposited onto the Si substrate with direct-current power of 120 W for 4 h. Prior to deposition, the substrate was ultrasonically cleaned in acetone, ethanol and deionized water sequentially. The sputtering chamber was vacuumed to a base pressure of 6×10^{-4} Pa. In order to guarantee homogeneity and improve the

bonding strength between film and substrate, the following parameters are maintained: the substrate rotation rate, 2 rpm; the pressure of argon gas, 0.2 Pa; and the substrate bias, −80 V. The deposition rate for the films was ~11 nm/min for CrCoNi and ~9 nm/min for VCoNi.

2.2. Mechanical and tribological tests

The hardness and elastic modulus of as-deposited films were measured using a Bruker Hysitron TI980 nano-indenter equipped with a diamond Berkovich tip. The maximum load was set to 10 mN at a constant loading rate of 2 mN/s, then kept at maximum load for 2 s, and unloaded at the same rate. To ensure the reliability of the results, 10 indentations with the interspacing of 20 μm were conducted. The maximum penetration depth was maintained always below 10 % of the total film thickness to avoid any substrate effect on the experimental results.

The ball-on-disk contact reciprocating mode (Bruker UMT tribolab) was adopted to conduct dry wear tests at room temperature, using GCr15 steel ball counterparts with a diameter of 6.35 mm. The normal load, reciprocating stroke, applied frequency and sliding time were fixed to 2 N, 1 mm, 1 Hz and 20 min, respectively. At least four independent tests were performed to avoid the contingency. The morphologies of the worn surface and wear rate were measured by 3D optical profilometry (Bruker Contour GT-K1).

2.3. Microstructural characterizations

The morphologies of the initial surface, cross-section and worn surface of films were examined using scanning electron microscopy (SEM, FEI Helios G4 OX). The compositional distribution of the initial microstructure and the worn tracks were analyzed by energy dispersive spectroscopy (EDS, Oxford X-Max^N). Transmission electron microscopy (TEM, FEI Talos F200X) was utilized to further identify the cross-sectional microstructures of initial and worn tracks. Slices for TEM were prepared by a focused ion beam (FIB, Helios G4 OX) using a standard lift-out technique. Furthermore, X-ray photoelectron spectroscopy (XPS, PHI 5000 VersaProbe III) was used to analyze the surface chemical states within the worn tracks by a monochromatic Al-K$_\alpha$ source. Three-dimensional elemental distribution at the atomic scale was determined using atomic probe tomography (APT) on a CAMECA LEAP 4000X HR instrument. Tip-shaped specimens for the 3D-APT tests were prepared using the focused ion beam (FIB) technique. The analysis was conducted in laser mode at a base temperature of 50 K, with a laser energy of 60 pJ at a pulse repetition rate of 200 KHz. The evaporation detection rate was set at 1 %, with an effective detection rate of 37 %. Following data acquisition, Imago Visualization and Analysis Software (IVAS) version 3.6.8 was employed for 3D reconstruction and compositional analysis.

2.4. Computational methodology

Molecular dynamics (MD) simulations were adopted to reveal the deformation behavior and surface segregation mechanisms from the atomic scale during friction. The initial model consists of an asperity and the nanocrystalline MPEA substrate comprising three elements with equimolar composition. The MPEA models with random solid solution structure possess the dimension of $300 \times 150 \times 150$ Å^3, comprising approximately ~600,000 atoms. The nanograins had random orientations and were uniformly distributed in each model. Although we acknowledge that the simplified nanocrystalline system in this study limits direct comparison to experimental structure, we firmly believe that atomistic simulations can effectively capture the underlying phenomena and provide a comparative trend between the CrCoNi and VCoNi systems, thereby offering valuable insights into the chemistry governing surface segregation within each columnar structure. The embedded atom method (EAM) potential was employed to elucidate the
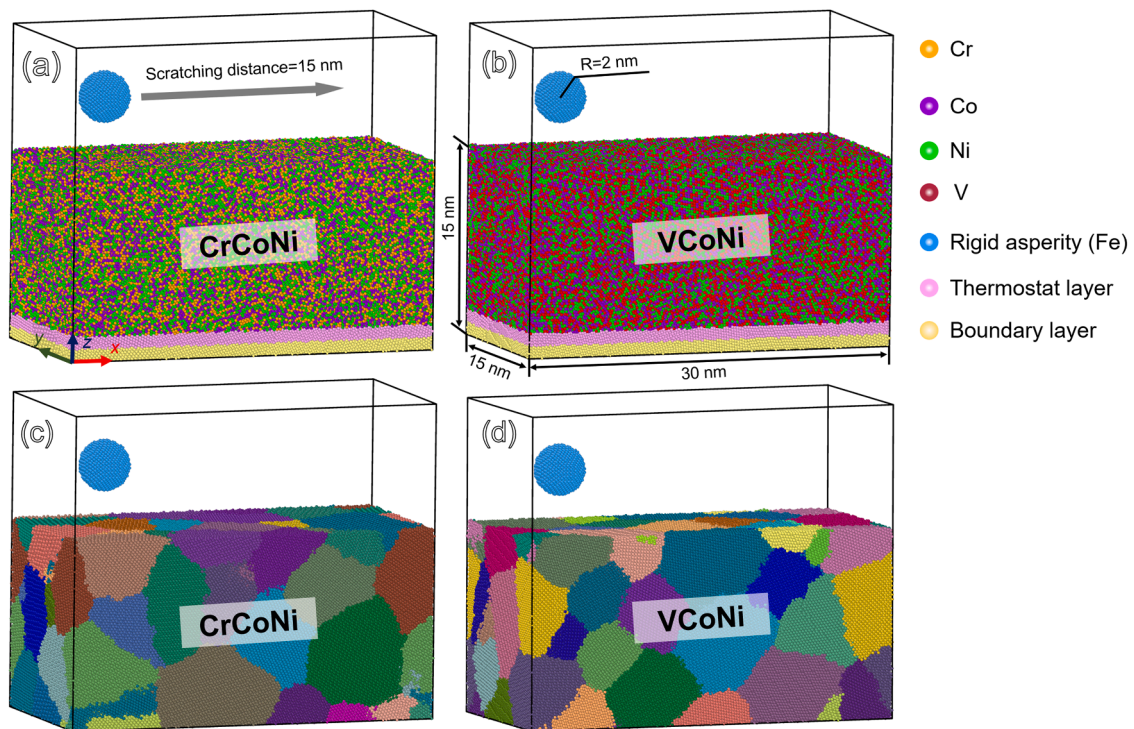
Fig. 1. The atomic model consisting of a tip and nanocrystalline MPEA: (a, b) Schematic of atomistic model for CrCoNi and VCoNi; (c, d) Different nanograins in CrCoNi and VCoNi represented by different colors.

metallic atom interactions in MPEA [30]. The Lennard-Jones (LJ) potential was used to describe the interactions between MPEA atoms and the sliding asperity, utilizing parameters derived from previous studies [31-33]. The simulations were conducted using the Large-scale Atomic/Molecular Massively Parallel simulator (LAMMPS) [34], and the visualization of structure and element distribution during sliding was demonstrated by the Open Visualization Tool (OVITO) [35].

The sliding simulation involved the division of the fully relaxed MPEA model into three distinct regions: a boundary atoms layer, a thermostat atoms layer, and a Newtonian atoms layer. The stability of the model was ensured by fixing a 1 nm thick boundary layer at the bottom, as illustrated in Fig. 1. In order to dissipate heat generated during the sliding process, a 1 nm thick thermostat layer was positioned above the boundary layer, which was maintained at a constant temperature of 300 K using the Langevin thermostat. The remaining atoms adhere to the principles of classical Newton's second law. The x- and y-directions were subjected to periodic boundary conditions, while a fixed boundary condition was imposed on the z-direction. Upon sliding, a micro-canonical ensemble (NVE) was adopted with a penetration depth of 1.5 nm, a sliding velocity of 100 m s^{-1} and a sliding distance of 15 nm for both models. The selected simulation parameters are a general approach that considers balancing computational efficiency and reliability [36-38]. For the sake of simulation convenience, a simplified Fe tip was selected to slide over the MPEA substrate as a representative of the steel counterpart.

3. Results

3.1. Microstructure of as-deposited mpea films

The microstructure and elemental distribution of the as-deposited MPEA films are shown in Fig. 2. For both MPEAs, as-deposited films with a thickness of 3 μm are successfully fabricated, showing columnar structures extending along the growth direction (Fig. 2a, d). The top surface morphologies from SEM (Fig. 2b, e) indicate the high quality of as-deposited films with circular fine grains, which are smooth, dense and

crack-free. Quantitative EDS analyses (Fig. 2c, f) reveal that the as-deposited MPEA films with equiatomic composition show a uniform distribution of alloying elements. To further assess the elemental distribution at atomic scale with sub-nanometer resolution, the 3D-APT experiments are conducted as illustrated in Fig. 2g. The results demonstrate a uniform distribution of Cr, Co, and Ni, being consistent with the SEM observation. The one-dimensional compositional profile (Fig. 2h) reveals that Cr, Co, and Ni concentrations are ~30 %, with little O detected which may be introduced from environment exposure during sample transfer [38]. Nevertheless, the uniform distribution of all elements suggests the absence of any significant segregation in the as-deposited sample.

As shown in Fig. 3, more detailed microstructure information of MPEAs was acquired by TEM. Fig. 3a and d show a typical low-magnification bright-field TEM image of the as-deposited MPEA films, in which columnar structures developed along the growth direction regularly. The selected area electron diffraction (SAED) patterns (the inset of Fig. 3a, d) identify the presence of single FCC phase for both films. The dark-field TEM image of the as-deposited MPEAs (Fig. 3b, e) further reveals the columnar structure with nano-grains inside. The distribution of columnar width (Fig. 3g, h), derived from >100 grains, yields an average column width of ~9.13 nm for VCoNi and ~15.35 nm in CrCoNi, respectively. A number of rod-like features (marked by red arrows) are found in the SAED pattern of CrCoNi (Fig. 3d), originating from the diffraction of numerous planar defects (e.g., stacking faults and twin boundaries). The HRTEM image, corresponding to FFT and IFFT analysis (Fig. 3f), confirms the presence of abundant stacking faults and nanotwin, when compared with the case of VCoNi (Fig. 3c). Attributed to the low stacking fault energy of CrCoNi, the formation of abundant planar defects during non-equilibrium preparation processes, such as rapid cooling of vapor deposition, is easily observed [39].

3.2. Mechanical and tribological properties

The mechanical properties of MPEA films were determined by nano-indentation tests. The hardness and Young's modulus were measured in
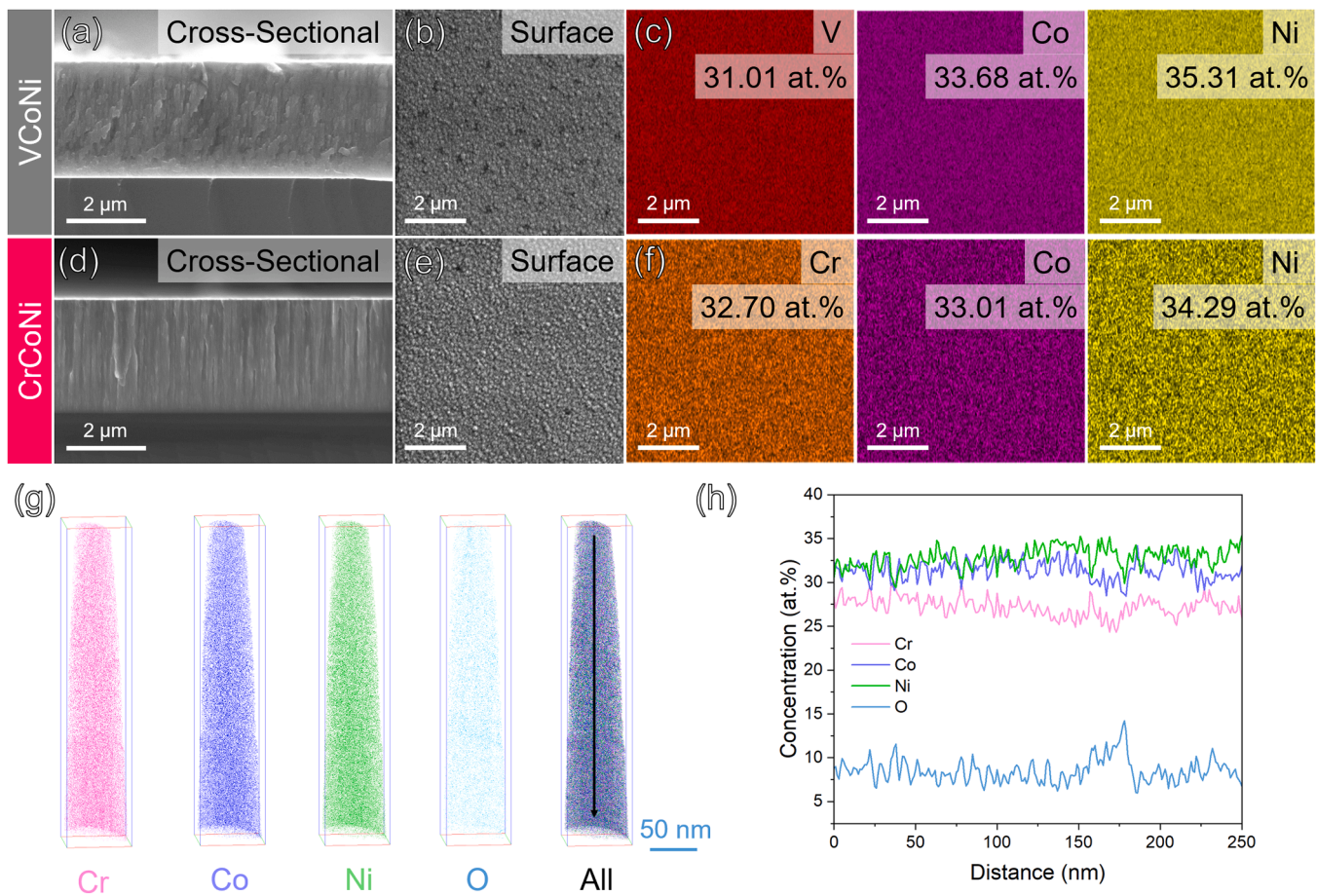
Fig. 2. Microstructure and elemental distribution of as-deposited MPEA films: (a, b) Cross-sectional and surface morphology of VCoNi film; (c) EDS mapping for as-deposited VCoNi film; (d, e) Cross-sectional and surface morphology of CrCoNi film; (f) EDS mapping for as-deposited CrCoNi film. APT results for the as-deposited film: (g) Atom maps reconstructed using 3D-APT that show the distribution of each element and (h) one-dimensional compositional profile (across the region indicated by the black arrow in (g).

a constant strain rate mode and the typical load-depth curves are shown in Fig. 4a. The maximum depth of indentation is <250 nm, i.e. lower than 1/10 of film thickness, which is typically considered free of substrate effects. Fig. 4b reveals that CrCoNi has a high hardness ($\sim$ 10.73 GPa), due to the presence of abundant planar defects with nanoscale spacing. Besides, the ratios of H/E and H^3/E^2, which are often employed to characterize the resistance of materials to plastic deformation and wear [40], were obtained as summarized in Table. 1. The CrCoNi film has higher values of H/E and H^3/E^2, demonstrating exceptional tribological properties from a purely mechanical perspective.

Fig. 5 shows the tribological properties of MPEA films at room temperature. The coefficient of friction (COF) rises rapidly and reaches a stable stage within 20 s. As shown in Fig. 5a, the COF of CrCoNi film is lower than VCoNi. The specific wear rate generated after sliding is obtained in Fig. 5b and the wear rate of CrCoNi film is 4.37×10^{-6} mm^3/(N·m), which is nearly half of that in VCoNi. Such a wear rate is extremely low for metallic alloys subjected to dry sliding wear [22]. The two-dimensional cross-sectional profiles obtained from the wear tracks of MPEA films are depicted in Fig. 5c, d. Notably, an obvious worn scar was formed on VCoNi surface when compared with CrCoNi with significantly shallower wear grooves. A comparison with the wear rates of other alloys, including CrCoNi alloys prepared by different techniques and recently developed wear-resistant MPEAs, is shown in Fig. 5e and f respectively. It is evident that the incorporation of nano-grains in CrCoNi effectively enhances the wear resistance of the film, surpassing that of existing CrCoNi alloys. In a parallel comparison with other MPEA films, the current CrCoNi exhibits a relatively low hardness in

comparison with other MPEA films, as shown in Fig. 5f. However, it demonstrates exceptional wear resistance comparable to certain refractory MPEA and carbide films.

The morphology and composition of wear tracks are revealed by SEM-EDS analyses in Fig. 6. VCoNi exhibits abundant microgrooves parallel to the sliding direction in the center of the wear track (Fig. 6a-c). According to EDS analyses, all alloying elements, i.e., V, Co and Ni, distribute uniformly in the wear track with slight oxidation (Fig. 6c and Table 2). The worn surface morphology of CrCoNi is characterized by a friction-induced oxide layer, accumulated wear debris, and transferred material from the counterface, forming distinct elevations on the surface (Fig. 6d-f), as detailed in the Supporting Information. Table 2 displays the quantitative EDS analyses of the wear tracks. The above analysis of wear tracks of MPEA film revealed both, abrasive and oxidation wear mechanisms, during the sliding process.

As shown in Fig. 7, the XPS analyses were used to characterize the elemental oxidation state observed within the wear tracks after sliding tests. The results illustrate the coexistence of an oxidized state of metal and a partial pure metallic state in each wear track. Notably, there is an obvious difference in the detection of oxygen elements. The proportion of OH$^-$ (532.13 eV) in the wear tracks of VCoNi is higher, caused by oxygen adsorption on the surface of the sample, while the proportion of metal oxide (530.53 eV) is only 22.3 %. However, the wear tracks of CrCoNi show a stronger peak of O^{2-}, accounting for 53.69 %. This observation suggests that a more extensive oxidation process took place within the sliding wear track of CrCoNi. In addition, it is worth noting that the relatively high content of H$_2$O and OH$^-$ on the sample surface is
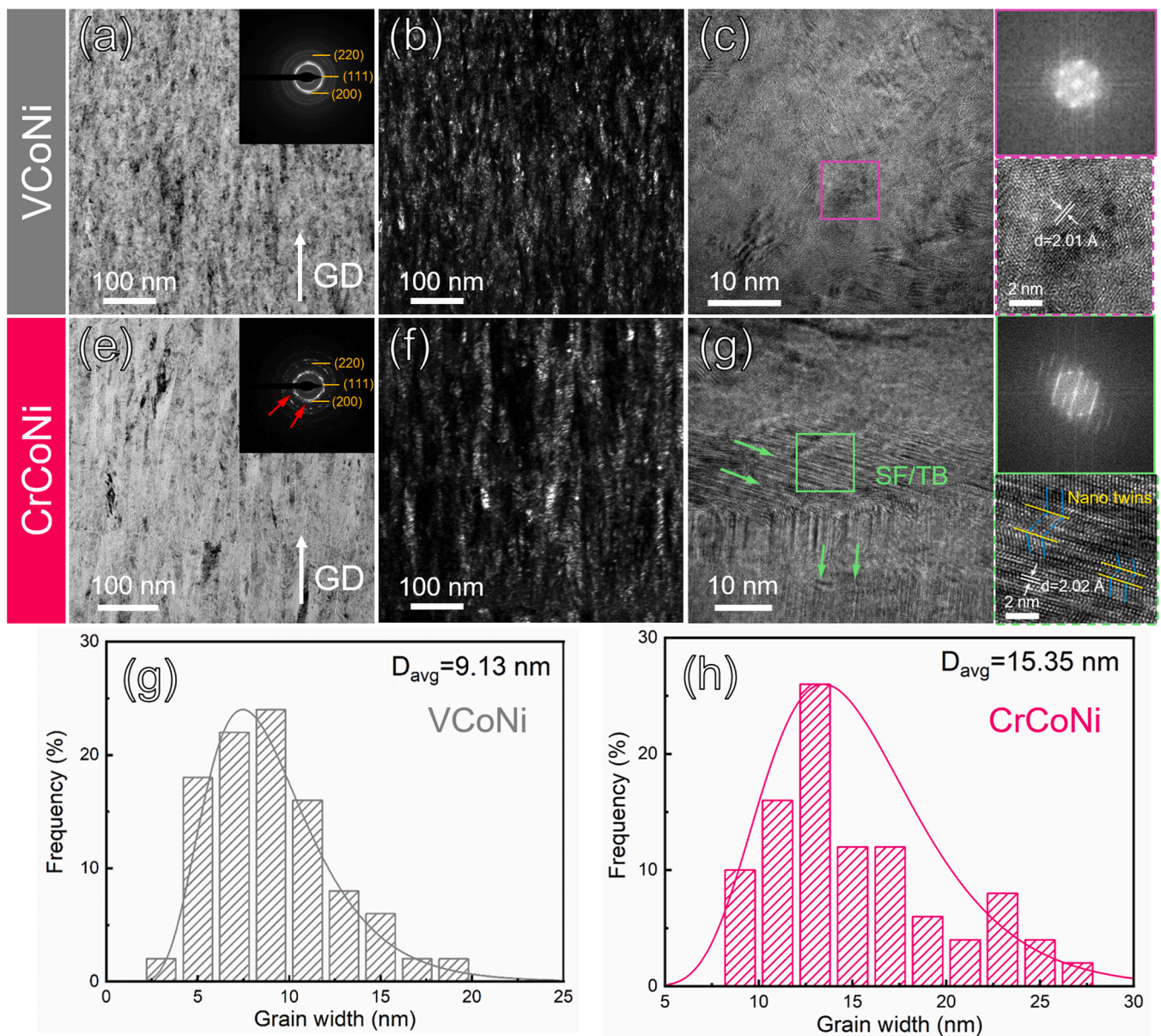
Fig. 3. Cross-sectional TEM observation of the as-deposited MPEA films: (a, d) Bright-field TEM images of as-deposited VCoNi and CrCoNi, with the inset showing the corresponding SAED patterns; (b, e) Dark-field TEM images of as-deposited VCoNi and CrCoNi; (c, f) HRTEM images for both films; (g, h) the statistical distributions of columnar width.

primarily due to high ambient humidity, which facilitates water vapor adsorption during sample preparation and transfer, despite the high vacuum conditions during thin film deposition. Friction experiments conducted in atmospheric conditions further promote the adsorption of H_2O and formation of OH^-. Given the shallow detection depth of XPS, typically ∼10 nanometers, surface contaminants such as adsorbed water molecules and hydroxyl groups are readily detected. While these factors introduce H_2O and OH^- signals into our XPS spectra, they do not affect our primary conclusion. The results demonstrate that CrCoNi surfaces exhibit a stronger metal oxide peak compared to VCoNi, indicating significant surface oxidation during the sliding process.

3.3. Friction-induced surface oxide layer and sub-layer microstructure

The cross-sectional microstructures of the wear tracks for VCoNi and CrCoNi films at room temperature were characterized by TEM in Figs. 8-9. A wear-induced gradient stress causes severe plastic deformation below the sliding surface and thus induces the formation of a gradient

nanostructure. For both films, the worn subsurfaces exhibit a distinct structural gradient, characterized by the presence of an oxide layer, sub-deformed layer, and matrix. However, the characteristics of the oxide layer exhibit dramatic differences for each case.

For the VCoNi film, there is an oxide layer with a thickness of only 10 nm below the sliding surface (Fig. 8a). The nano-columnar structures are progressively refined and bent in sub-layer with a thickness of ∼70 nm towards the sliding direction, as can be recognized in the HAADF image. To reveal more detailed chemical and structural information for the oxide layer, a representative area was selected for EDS and HRTEM analyses. The EDS element mappings (Fig. 8b) reveal that oxygen and the alloying elements are uniformly distributed in the oxide layer (marked by the white dotted line), indicating uniform oxidation during sliding. The characterization of the subsurface structure is shown in Fig. 8c. The HRTEM image (Fig. 8d) clearly exhibits a disordered amorphous structure and a typical amorphous halos ring (inset of Fig. 8d) from fast Fourier transforms (FFT) of the HRTEM images. Furthermore, HRTEM analysis of the sub-layer (Fig. 8e) reveals the
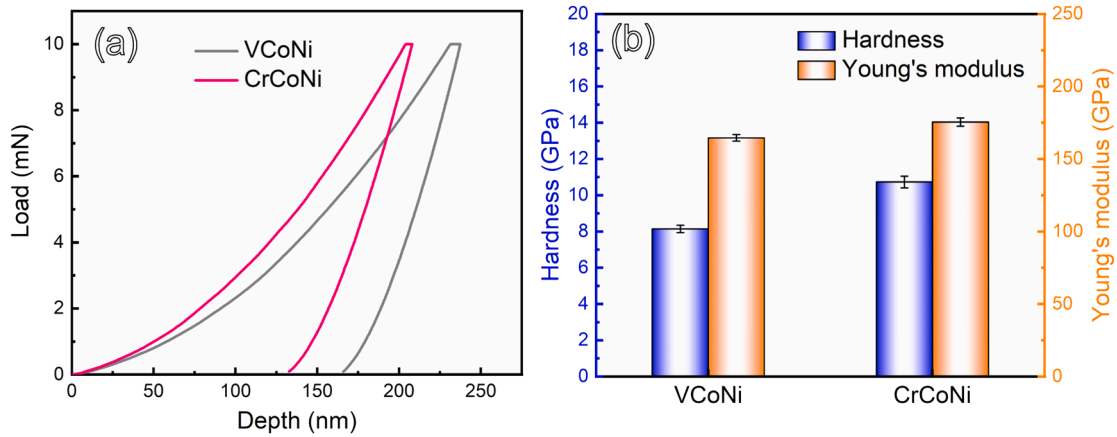
Fig. 4. Nanoindentation behaviors of MPEA films: (a) Typical load-depth curves for VCoNi and CrCoNi; (b) Measured hardness and Young's modulus of VCoNi and CrCoNi.

Table 1
Summary of mechanical properties of MPEA films.

Sample	Hardness (GPa)	Young's modulus (GPa)	H/E	H^3/E^2 (GPa)
VCoNi	8.31 ± 0.20	164.55 ± 2.26	0.0505	0.0212
CrCoNi	10.73 ± 0.32	175.50 ± 2.84	0.0611	0.0409

presence of ultrafine nanocrystalline structures with a grain size of ~4 nm. On the other hand, the diffraction rings are more continuous, indicating the random orientation of nanograins as a result of extensive grain size refinement within this plastic deformation layer. A wear-induced gradient stress causes severe plastic deformation below the sliding surface and thus the columnar structure are gradually refined and bent upon sliding [22]. As the crystallographic spacing (~2.06 Å) of the FCC nanograins is quite close to the base VCoNi film (~2.01 Å), it can therefore be concluded that the sub-layer is evolved from the original VCoNi phase after experiencing severe plastic deformation.

For the CrCoNi film, a much thicker oxide layer of ~50 nm is built up beneath the sliding surface (Fig. 9a and c). It is found that Ni concentration in the oxide layer (~48.79 %) increases relative to the normal concentration in the film (~34.29 %), as revealed by EDS element analysis (Fig. 9b), highlighting an intriguing selective oxidation behavior upon friction. The HRTEM image (Fig. 9d) shows a nanocomposite structure with nanograins embedded in the amorphous matrix of the oxide layer. The FFT analysis was carried out to identify the specific crystalline structure (nanograin region marked by d1 and amorphous region marked by d2). The FCC structure in region d1 can be clearly distinguished. Additionally, the crystalline plane spacing of nanocrystalline grains was measured to be ~2.48 Å, being close to the (111) spacing of NiO [66]. There are no obvious diffraction spots in region d2, but rather a typical amorphous halos ring. The average size of nanocrystalline particles in the oxide layer is ~6.23 nm, as displayed in Fig. 9e. More specifically, the HRTEM image, its corresponding FFT image, and EDS analysis (Fig. 9g and f) also confirm the presence of a Ni-rich crystalline phase within the amorphous matrix.

It is important to note that the surface of CrCoNi undergoes severe oxidation, which enables the glaze layer to accommodate most of the wear-induced plastic deformation. As a consequence, the deformed sub-layer of CrCoNi (15 nm) is significantly thinner than that of VCoNi (70 nm). Nevertheless, the occurrence of FCC to HCP phase transformation is observed within this deformed sub-layer of CrCoNi, as confirmed by both the FFT (Fig. 10b) and IFFT (Fig. 10c) images, whereas no such transformation is observed in VCoNi. Another TEM image (Fig. 10d and e) taken from the region below the nanocomposite layer of CrCoNi reveals the elongated grains with a thickness of ~6 nm parallel to the sliding direction, indicating the structure refinement in the sub-layer

being similar with VCoNi. Moreover, strip structures consisting of multiple stacking faults are frequently observed within these deformed grains, as shown by the HRTEM and FFT in Fig. 10f. Owing to its low SFE, the propensity for stacking faults and FCC→HCP phase transformation is increased in CrCoNi under severe loading conditions [67]. The occurrence of stacking faults and phase transformations during sliding in CrCoNi has also been confirmed through MD simulation. Simulations conducted over the same sliding distance for both CrCoNi and VCoNi reveal significant HCP phase transformations in the subsurface of CrCoNi, whereas only minor slip events are observed in VCoNi, as shown in Fig. 10g and h. Fig. 10i presents the Generalized Stacking Fault Energy (GSFE) calculated for both CrCoNi and VCoNi systems. The GSFE values obtained from the MD simulations are -4.2 mJ/m^2 for CrCoNi and 20.9 mJ/m^2 for VCoNi. Owing to its negative SFE, the propensity for stacking faults and FCC→HCP phase transformation is increased in CrCoNi under severe loading conditions [67]. Accordingly, the congruence between molecular dynamics (MD) simulations and experimental outcomes delivers compelling evidence, thereby reinforcing our conclusions concerning the structural behavior of CrCoNi during sliding process.

4. Discussion

The present study systematically investigated the dry sliding wear behaviors of MPEA films with nanograined structure against GCr15 friction pair at room temperature, specifically focusing on elucidating the wear mechanism, sliding-induced element redistribution, and oxide layer formation. The study yielded several intriguing findings: (i) Sliding wear induces the redistribution of nickel within the surface region of CrCoNi at room temperature; (ii) A nanocomposite with an amorphous-crystalline structure forms on the surface of CrCoNi, whereas a purely amorphous surface is generated on the surface of VCoNi; (iii) The dynamically formed amorphous-crystalline oxidative surface endows superior wear resistance to CrCoNi compared to most MPEA films. Thus, the following discussion will focus on the factors governing these phenomena in CrCoNi films during sliding wear at room temperature.

4.1. Element redistribution upon friction

Element redistribution is a well-documented phenomenon during prolonged aging treatments [68,69], while reports on element redistribution induced by friction are scarce. Previous studies have also identified shear-induced Y segregation in Fe-based bulk metallic glass at room temperature during wear tests [70]. The above study, supported by first-principles calculations and classical molecular dynamics simulations, elucidate that the segregation is triggered by significant atomic
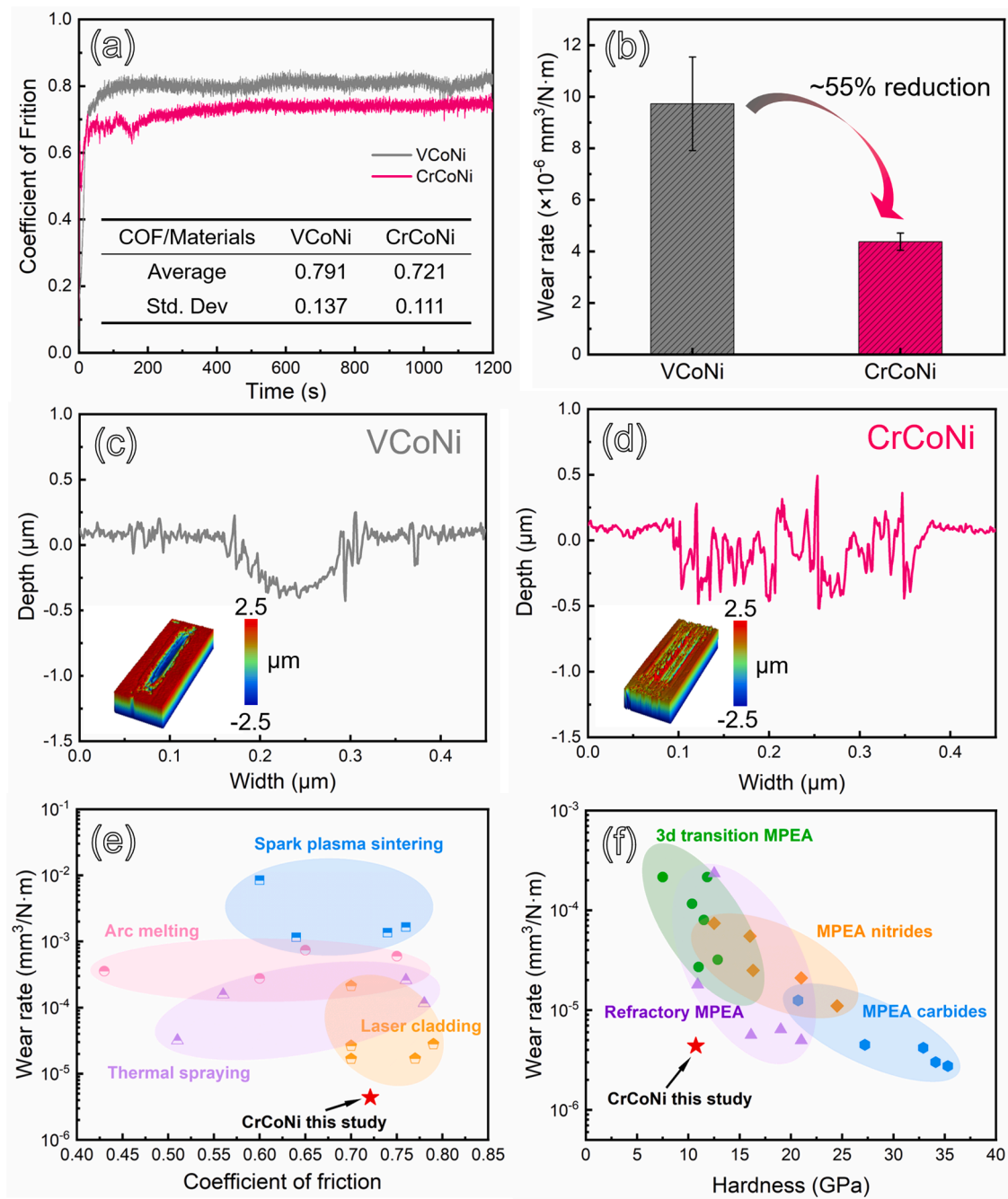
Fig. 5. Tribological properties of MPEA at room temperature: (a) Coefficient of friction versus sliding time; (b) Specific wear rate of VCoNi and CrCoNi; (c, d) 2D cross-sectional profiles of the wear tracks; (e) Comparison of wear rate between CrCoNi alloys prepared by different techniques. Data are selected for CrCoNi under dry friction at room temperature from Refs. [8,41-54]; (f) Comparison of wear rate between MPEA films. Data are selected for films prepared by magnetron-sputtering under dry friction condition from Refs. [20,55-65].

size differences in bulk metallic glass systems. However, in our CrCoNi system, the atomic sizes are quite similar, differing by only a few percent, compared to the ~10 % difference observed in the bulk metallic glass systems from the study [70]. Therefore, the size segregation mechanism identified in those systems does not apply to our work. In addition, it's noteworthy that the structure in the referenced study was amorphous, whereas our research focuses on crystalline CrCoNi films. Our research aims to further investigate element redistribution induced by friction in crystalline systems with the similar atomic sizes, thereby broadening the understanding of different segregation mechanisms across various material systems. Revealing the intrinsic factors responsible for element redistribution and segregation of nickel on the surface

after sliding is crucial for comprehending the structural characteristics of the worn surface. Intrinsically, it is widely acknowledged that Ni-Ni short-range order (SRO) represents the favored bonding between adjacent atomic pairs in a CrCoNi solid solution system. Heretofore, predicted simulation and direct observation of SRO in Ni-based FCC MPEA were achieved and the preliminary origin for local SRO has been attributed to multiple sources, including enthalpy-driven bonding as well as magnetic and/or electronic interactions between components [71]. Currently, the enthalpy of mixing between atomic pairs serves as a quantitative indicator of SRO, reflecting the bonding energy (i.e., stronger interaction corresponds to more negative mixing enthalpy). In current research, it is considered that VCoNi has a stronger tendency for
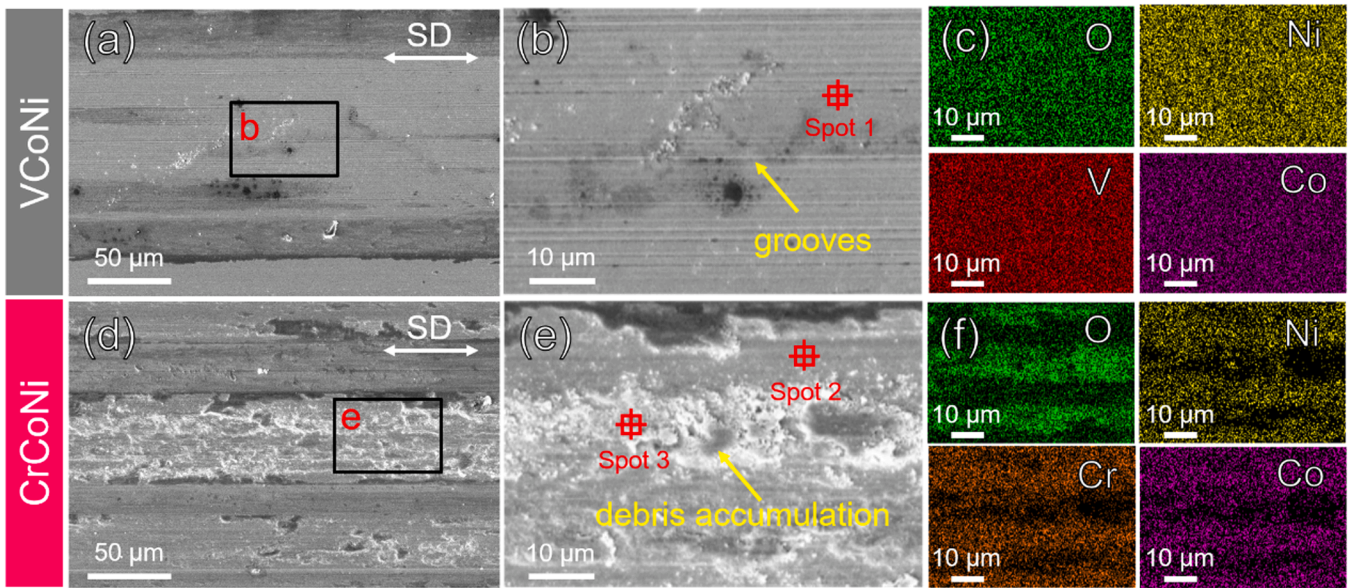
Fig. 6. Surface morphologies and composition of wear tracks: (a, b) SEM images of worn surface of VCoNi; (d, e) SEM images of worn tracks of CrCoNi; (c, f) Corresponding EDS mapping of the worn region.

Table 2
Quantitative EDS analysis of the wear tracks.

	V (at.%)	Cr (at.%)	Co (at.%)	Ni (at.%)	O (at.%)
Spot 1	27.23 ± 0.27	—	29.20 ± 0.36	30.07 ± 0.38	13.49 ± 0.30
Spot 2	—	27.01 ± 0.29	26.65 ± 0.37	27.70 ± 0.40	18.64 ± 0.15
Spot 3	—	19.80 ± 0.33	16.50 ± 0.43	17.31 ± 0.45	46.39 ± 0.26

SRO [72], partly due to the negative mixing enthalpy of VCoNi system compared with CrCoNi. Specifically, the more negative mixing enthalpy of V-Ni pairs (−18.0 kJ/mol) than Cr-Ni pairs (−6.7 kJ/mol) leads to the preferential bonding of V-Ni towards a thermodynamically stable structure in VCoNi [73,74]. It is also known that the presence of electronic transference is conducive to chemical bonding. Nutor et.al [75] demonstrated that V in VCoNi donates an average of 0.63 electrons/atom, with Ni accepting 0.34 electrons/atom and Co accepting 0.29 electrons/atom. In CrCoNi, Cr donates an average of 0.41 electrons/atom, from which 0.25 electrons/atom are accepted by Ni and 0.16 electrons/atom by Co. The enhanced charge transference in V-Ni pairs is evidently responsible for the stronger bonds and increased structural stability, thereby preventing potential Ni segregation during sliding.

On the other hand, the mechanism underlying sliding-induced surface Ni segregation of CrCoNi during deformation is comprehended through MD simulation. The compositional distribution of the contact region is quantified before and after sliding in both models. The atom in direct contact was defined as the one exclusively expelled by the tip, while the remaining atoms attracted by the tip formed an adhesive region at subsurface [76,77]. Typically, the contacting atoms are commonly removed and squeezed out of the worn scar during sliding, while the atoms in adhesive regions participate in subsurface compositional reconstruction. According to previous studies, a critical distance
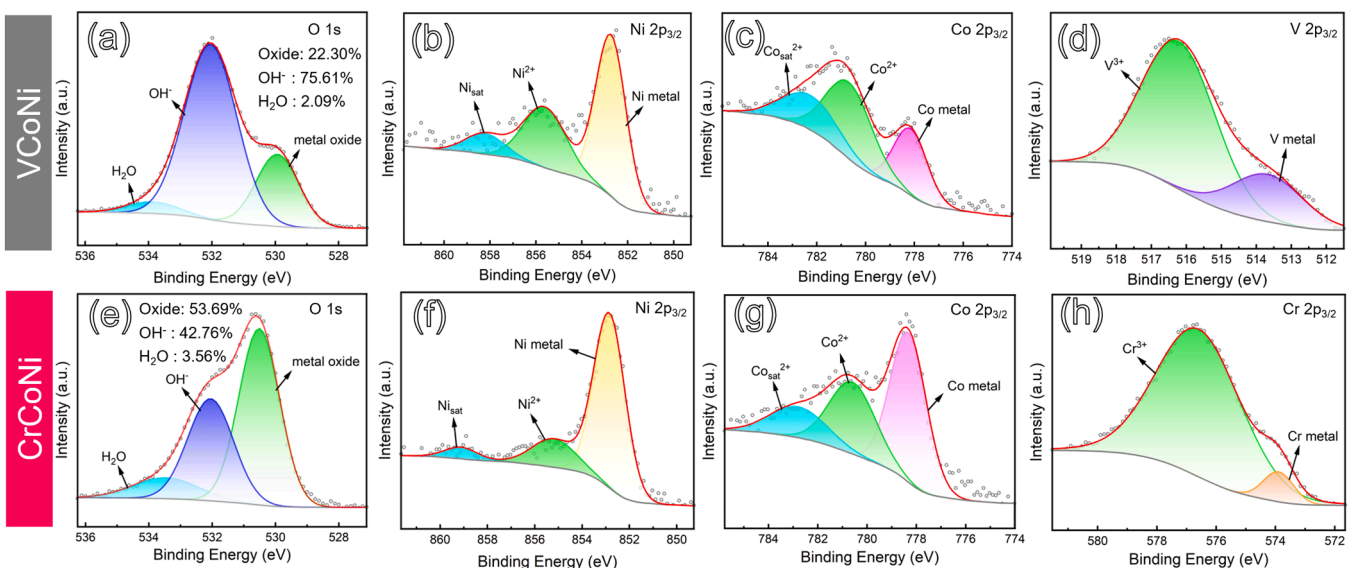

Fig. 7. XPS spectra from wear tracks after sliding tests: (a-d) VCoNi; (e-h) CrCoNi.
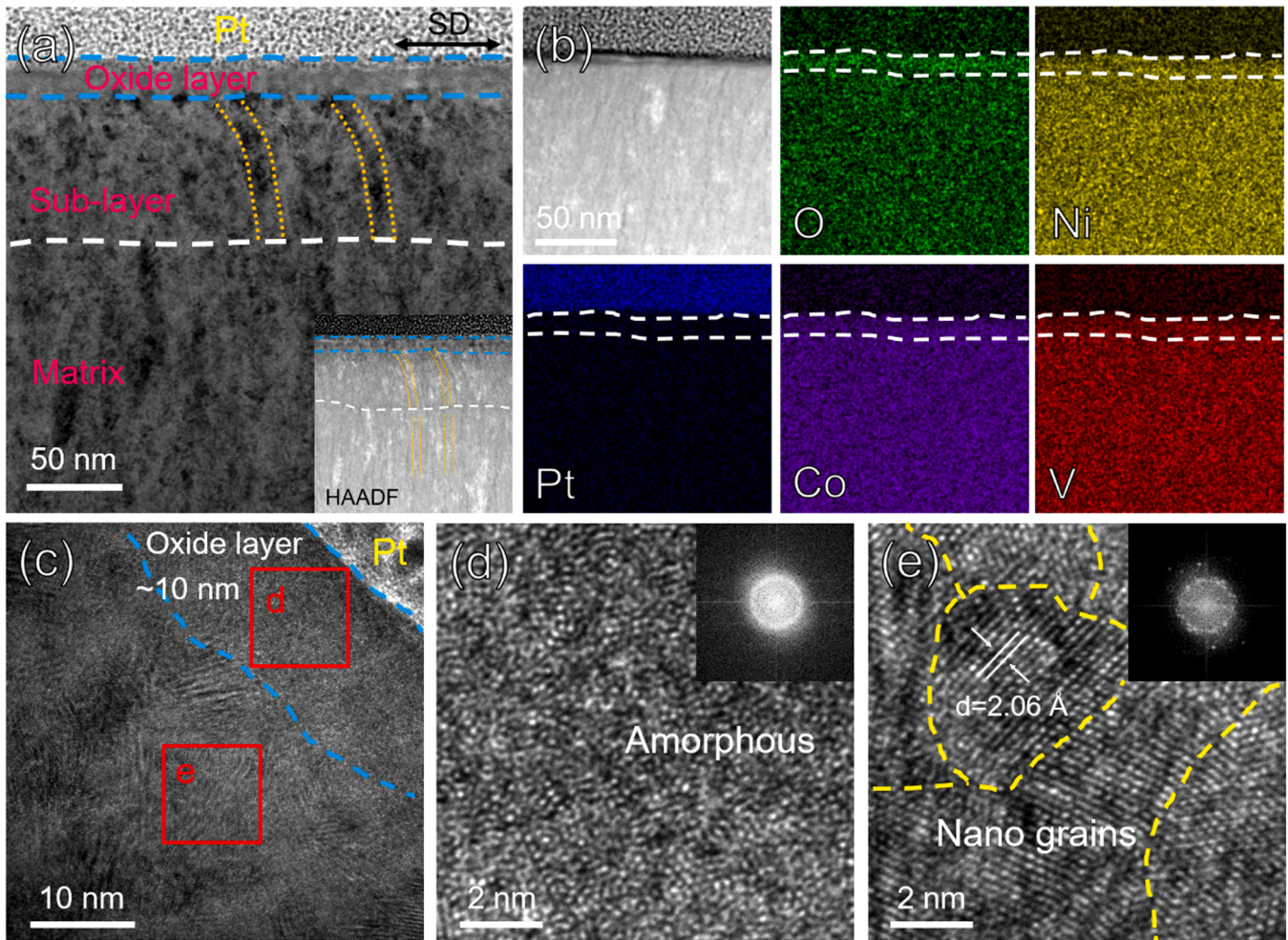
Fig. 8. ND-SD cross-sectional TEM characterizations of VCoNi after sliding: (a) Bright field TEM image of subsurface microstructure, with the inset showing the corresponding HAADF image of the plastic deformation region; (b) Typical HAADF-STEM image and corresponding EDS elemental distribution in the subsurface. (c) HRTEM image of the subsurface; (d) HRTEM image of the amorphous structure in oxide layer with the inset showing the FFT pattern; (e) HRTEM image of nanograins in sub-layer with the inset showing the FFT pattern.

of $2^{1/6}\sigma$ was defined to distinguish the contact and adhesive regions beneath the tip, where σ is the distance scale used to describe the interaction between the metallic surface and tip [76,77]. It is noticed here that σ_{Ni-Fe} was selected as a reference due to its minimal interatomic distance and convenience for the analysis for Ni reconstruction. The atoms whose distances are $<2^{1/6}\sigma_{Ni-Fe}$ away from the tip are often removed and squeezed out of the worn scar during sliding, while the adhesive atoms whose distances range from $2^{1/6}\sigma_{Ni-Fe}$ to cutoff radius formed adhesive regions. Subsequently, we partition the adhesive atoms interacting with the indenter into several layers to discern the specific elemental distribution based on the following definition, wherein the distance between layer N of adhesive atoms and indenter is obtained as $d_N = 2^{1/6}\sigma_{Ni-Fe} + (N-1) R_a$, where R_a is the average diameter of constituent atoms (Fig. 11a). The presence of slight nickel segregation can be clearly observed in the first layer after indentation contact (Fig. 11b), while the composition fluctuated around the equal-atomic ratio in the remaining adhesive layers located further away from the indenter. The segregation became significant after friction with a proportion of ~45 % Ni observed in the first adhesive layer (Fig. 11c). Meanwhile, the atomic proportions in the rest adhesive layers were close to the initial state. Such phenomena, however, were not observed in the VCoNi system (Fig. 11d, e).

The underlying mechanism governing the elemental redistribution was further elucidated. Firstly, the difference in the pairwise interactions for Cr-Fe, Co-Fe, V-Fe and Ni-Fe came into mind. Considering

the possible effect of adopted potential function between tip and MPEA, we conducted an additional simulation to use a diamond C tip, in which the energy and distance parameters of the LJ potential were changed to Cr-C, Co-C, V-C and Ni-C [78]. The atomic proportions, as shown in Fig. S1 and Table S1, are very close to the results presented in Fig. 11 (a)-(d), suggesting that any disparity in pairwise interactions between the substrate and indenter atoms is negligible.

Furthermore, the ambient sliding experiments in the nitrogen atmosphere were conducted to confirm the unique friction-induced Ni segregation and exclude the oxidation effect. The cross-sectional HAADF-EDS analysis after sliding in a nitrogen atmosphere (Fig. S2) shows that the deformed layer (~50 nm) exhibits significant structural evolution and elemental segregation. Obviously, there is a Ni segregation layer (~30 nm) at the topmost surface, while the underlying deformation layer is a segregation-free layer (~20 nm). However, there is an unavoidable introduction of oxygen in a nitrogen atmosphere, as shown by EDS elemental mapping (Fig. S2). Oxygen in CrCoNi films during sliding likely originates from target material oxidation, residual oxygen in the deposition chamber, air exposure during sample handling, and measurement inaccuracies. Despite these sources, the oxygen content was low (~10 %), with minimal impact on tribological performance. The significant increase in oxygen content in the friction-induced oxide layer (~40 %) during wear tests highlights oxygen's role in modifying friction layer properties. Nitrogen's low reactivity
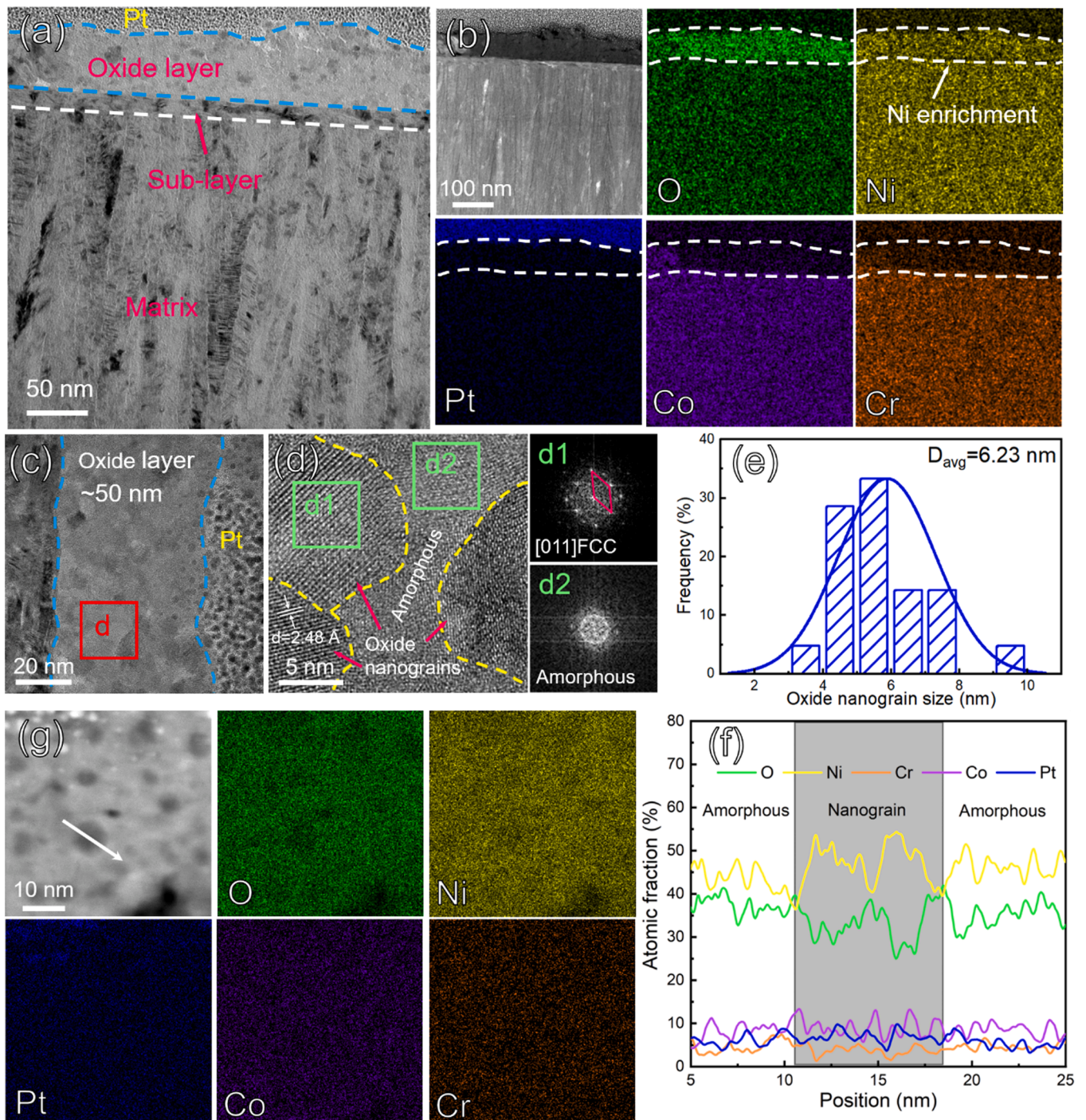
Fig. 9. ND-SD cross-sectional TEM characterizations of CrCoNi after sliding: (a) Bright field TEM image of the worn subsurface microstructure; (b) Typical HAADF-STEM image and corresponding EDS elemental distribution of the subsurface; (c) HRTEM image of the topmost oxide layer; (d) HRTEM image of amorphous-crystalline nanocomposites structure with the FFT pattern of amorphous and nanograin regions; (e) Statistical distribution of nanograin size in oxide layer; (g) A HAADF-STEM image and corresponding EDS elemental mapping of the oxide layer; (f) Line profiles of element distribution along the white arrow in (g).

under test conditions accounts for its absence in the measurements. Therefore, minor oxygen contamination has an insignificant impact on friction-induced oxide layers and Ni segregation during wear performance. Therefore, we believe that the chemical evolution may be closely related to the frictional-induced gradient strain, similar to the structural stratification caused by cycling friction [79,80]. The abundant defects introduced at the topmost surface will expedite the atomic diffusion/rearrangement and surface segregation behavior of Ni. These experimental results coincide with the atomic simulation, thereby ruling

out the influence of oxidation on Ni segregation. It is noteworthy that the Ni-rich layer in air is thicker than that in nitrogen, attributed to the fact that the introduced abundant defects provide diffusion pathways for the environmental O to contribute to the formation of a thicker oxide layer. To identify the role of nanograins on Ni segregation during friction process, CrCoNi with coarse grains were fabricated (Fig. S3) and then slided in a nitrogen atmosphere. The corresponding cross-sectional HAADF-EDS mappings (Fig. S4) reveal that elemental segregation is absent in the deformed layer after sliding tests. Therefore, it is confirmed
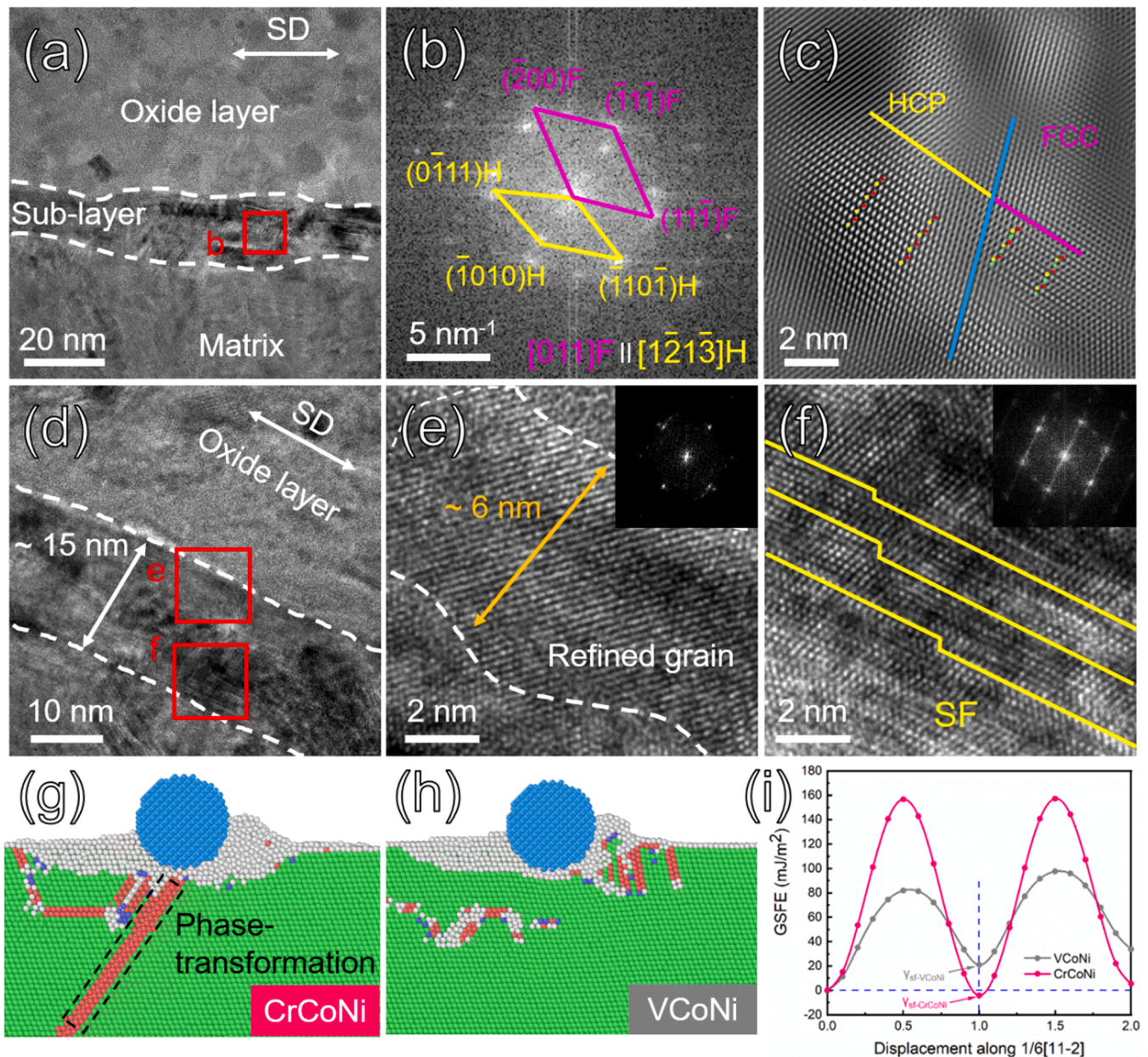
Fig. 10. TEM observation and MD simulation for the phase transformation of CrCoNi after sliding: (a) A high-magnification TEM image showing the structure of deformed sub-layer; Corresponding (b) FFT and (c) IFFT images for the red-boxed region in (a); (d) A local TEM image taken from the sub-layer, showing the cyclic sliding-induced structure refinement and defects; (e-f) HRTEM images of the selected area marked in (d) with the corresponding FFT images shown inset; The evolution of atomic structure for (g) CrCoNi and (h) VCoNi during friction; (i) The generalized stacking fault energy (GSFE) of both models at 273 K. (For interpretation of the references to colour in this figure legend, the reader is referred to the web version of this article.)

that nanograins play an essential role in promoting Ni segregation, due to its metastable microstructure with massive grain boundaries and defects induced by non-equilibrium magnetron sputtering.

Based on above analysis, we believe that the Ni segregation is driven by the thermodynamic force rather than the tip and environment effects. We then calculated the potential energy of the reconstructed system with surface segregation. Taking CrCoNi as an example (Fig. 12a), new models with surface composition in the first and second layers that exactly match those obtained after indentation and scratching are constructed. The models have a size of $58 \times 50 \times 30$ Å^3 and the specific surface element proportion is presented in Table 3. The configurations were subjected to periodic boundary conditions in the X and Y directions, while the Z direction was kept fixed. Then, the potential energy was determined through energy minimization for both the CrCoNi and

VCoNi systems (Fig. 12b, c). The sequential decrease in potential energy observed after indentation and scratching for CrCoNi clearly indicates a more stable configuration with surface nickel redistribution. Instead, inconspicuous changes in potential energy are observed in VCoNi without any distinct redistribution of elements. In addition, as noted in Fig. S5 (Supplementary materials), during the sliding process, the temperature in front of the sliding indenter increases significantly. It can be speculated that this thermal effect also promotes the elemental redistribution during sliding friction.

The above thermodynamic analysis indicates that the redistribution behavior of elements in CrCoNi may be attributed to the disparities in surface energy among Cr, Co, and Ni, as displayed in Table 4. It is worth noting that the surface energy of Ni is comparatively lower than that of Co and Cr, leading to a tendency for Ni segregation at the surface. It is
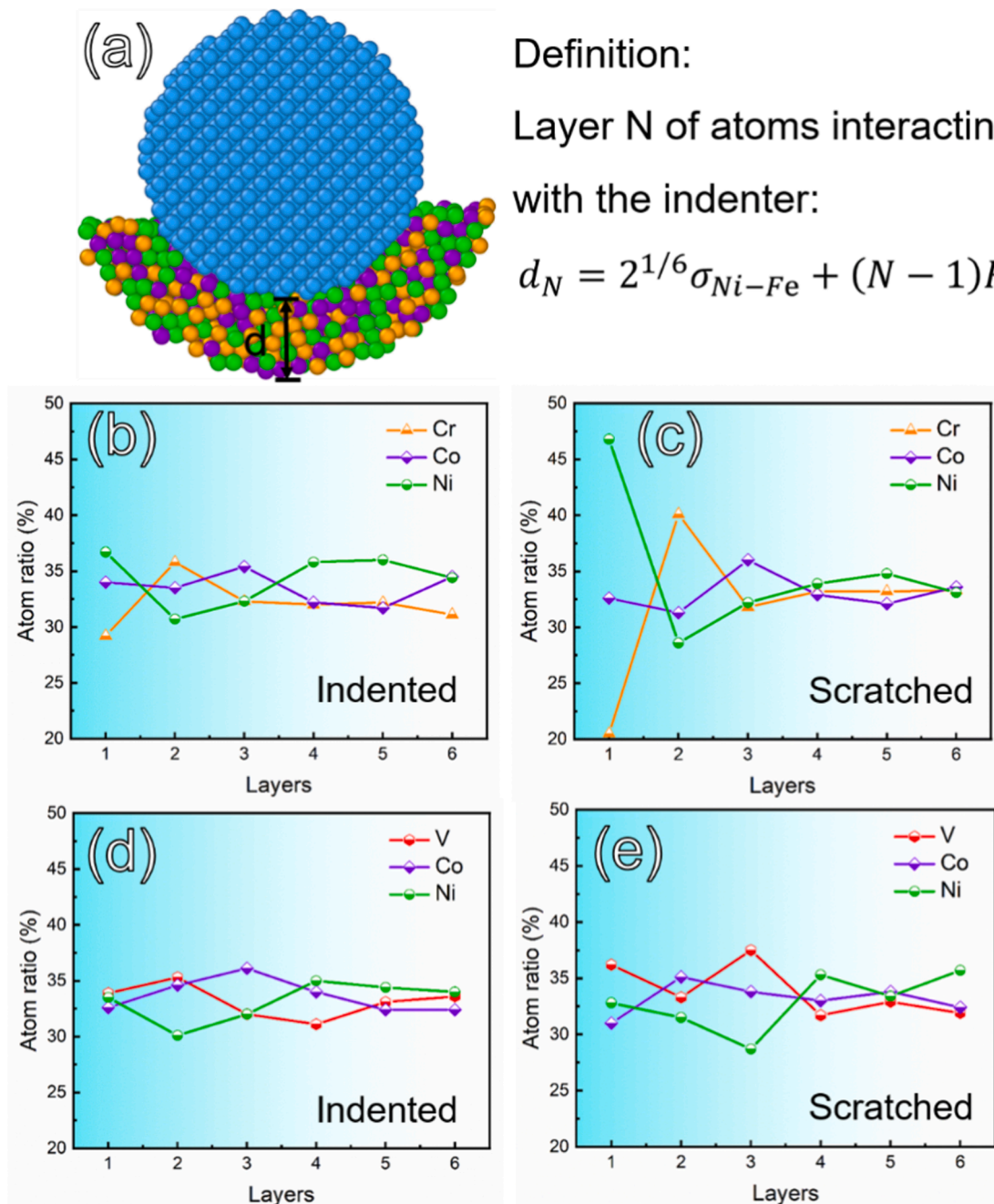
Fig. 11. The element distribution of MPEA after indentation and scratching: (a) Schematic diagram showing the definition of adhesive atoms; The atom ratio in CrCoNi (b) before and (c) after sliding; The atom ratio in VCoNi (d) before and (e) after sliding.

also noted that the observed friction-driven surface rearrangement is distinct from the long-range diffusion that occurs during high temperature oxidation of CrCoNi, where surface segregation and oxidation of Cr atoms are evident due to its higher diffusion coefficient [68,69,81]. In general, friction tends to generate heat and may contribute to elemental diffusion. The local flash temperature on the worn surface was estimated to be 640 K (the calculation details can be found in the Supplementary note). It can be seen that in the present work, the reciprocating sliding with low transient flash heating and short time is not sufficient to provide an effective driving force for elemental diffusion compared to high-temperature aging. Flash heating may not be the dominant factor for the elemental segregation on the worn surface during the sliding.

On the other hand, upon tribological loading, the contacting asperity will introduce tensile stress at its trailing edge [82], which may enhance the atomic displacement for composition change. Obviously, as the worn surface undergoes repeated sliding, this cyclic stress will lead to the accumulation of shear strain at the surface, thereby promoting atomic motion or shuffling that is necessary for reducing the overall potential energy. From a kinetic perspective, it is believed that frictional stress plays a pivotal role in the elemental redistribution of Ni in the CrCoNi alloy.

4.2. Formation of an amorphous-crystalline oxide surface

Overall, we adopted molecular dynamics simulation to analyze the surface elemental redistribution behavior of MPEA during sliding friction, revealing a significant reduction in potential energy. Here, we further elucidated the formation of an oxidative surface on the basis of
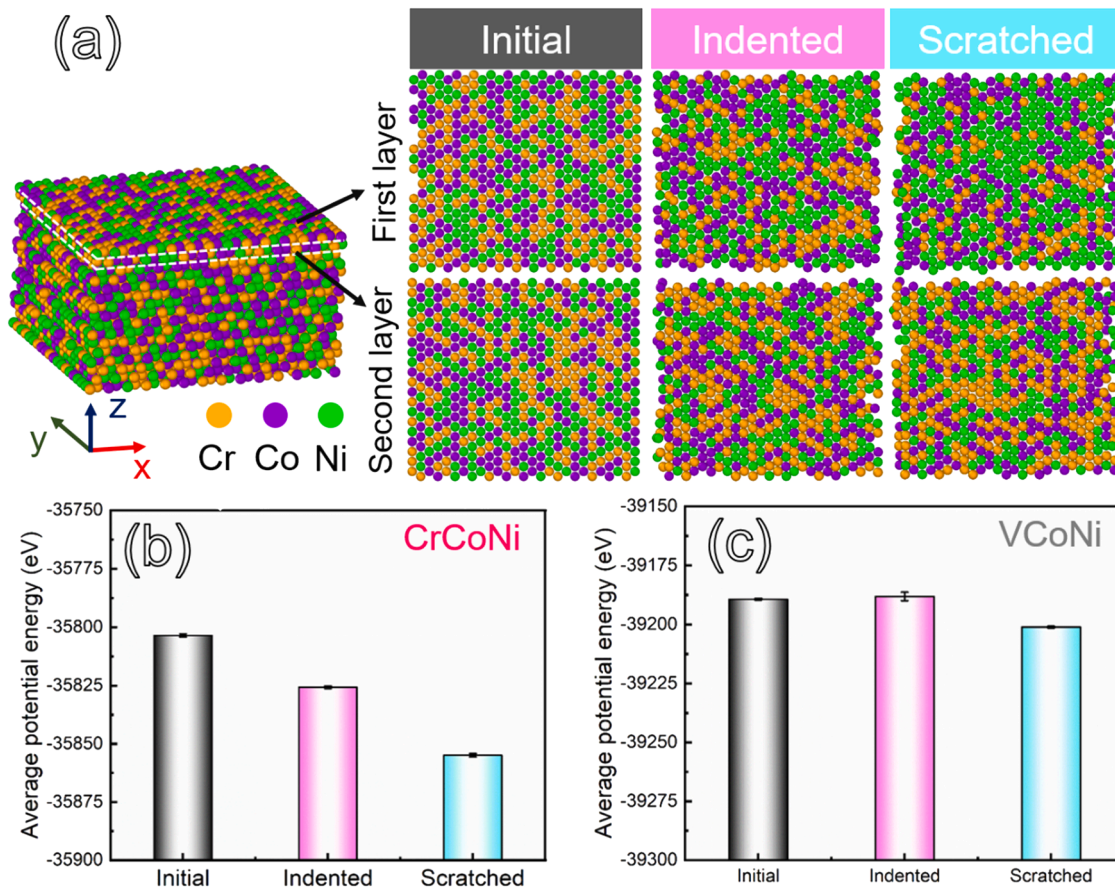
Fig. 12. Potential energy of MPEA with surface segregation: (a) Schematic diagram of potential configuration of CrCoNi; (b, c) Average potential energy of CrCoNi and VCoNi with initial, indented and scratched surface composition.

Table 3
The specific surface element proportions of each configuration and the calculated potential energy.

CrCoNi					Potential energy (eV)
State		Cr (at. %)	Co (at. %)	Ni (at. %)	
Initial	Layer 1	33.3	33.3	33.3	−35,803.5
	Layer 2	33.3	33.3	33.3	
Indented	Layer 1	29.2	34.0	36.7	−35,825.7
	Layer 2	35.8	33.5	30.7	
Scratched	Layer 1	20.5	32.6	46.8	−35,854.9
	Layer 2	40.1	31.3	28.6	

VCoNi					Potential energy (eV)
State		V (at.%)	Co (at.%)	Ni (at.%)	
Initial	Layer 1	33.3	33.3	33.3	−39,189.3
	Layer 2	33.3	33.3	33.3	
Indented	Layer 1	33.9	32.6	33.5	−39,188.1
	Layer 2	35.3	34.6	30.1	
Scratched	Layer 1	36.2	31.0	32.8	−39,201.1
	Layer 2	33.3	35.1	31.5	

Table 4
Comparison of surface energy for Cr, Co, V and Ni elements [83].

Element	lattice structure	Surface	Surface energy (J/m^2)
Cr	BCC	(100)	3.98
	BCC	(110)	3.51
Co	HCP	(0001)	2.78
V	BCC	(100)	3.03
	BCC	(110)	3.26
Ni	FCC	(100)	2.43
	FCC	(111)	2.01

sliding, the nanocrystalline structure of the MPEA film undergoes further refinement as a result of dislocation and defect accumulation at the surface, leading to an increase in the system's free energy. Once the critical value of free energy is reached, the crystal would collapse into an amorphous structure [9,86]. This process should be promoted in VCoNi with a complex composition and significant lattice distortion [87]. Besides, the local friction heat can boost the oxidation behavior on the film [88], wherein the abundant grain boundaries serve as pathways for the ingress of oxygen. According to the empirical law of glass forming ability, a mixture of small O atoms into alloys leads to a modification in atomic coordination with significant differences in atomic size and a more negative mixing enthalpy of the system. This leads to the formation of amorphous oxides on the surface [26,89].

As for CrCoNi, the segregation of Ni elements occurs on the surface, wherein the Ni will be oxidized preferentially, forming NiO nano-oxide. This depends on the fact that the oxidation activation energy of Ni is lower than that of MPEA alloy, (i.e., pure Ni:100 kJ/mol, CrCoNi: 277.9 kJ/mol) [81,90]. Given the sluggish diffusion effect in MPEA, it is

this elemental redistribution.

After friction, a composited structure with an amorphous-crystalline oxide layer was observed on the surface of CrCoNi, whereas VCoNi exhibited a distinctively pure amorphous structure. In this study, the occurrence of a crystalline-to-amorphous transition during friction for MPEA is ascribed to the synergistic effects of mechanical deformation and oxidation. Solid-state amorphization can be generally achieved through high-strain mechanical deformation [84,85]. Upon sustained
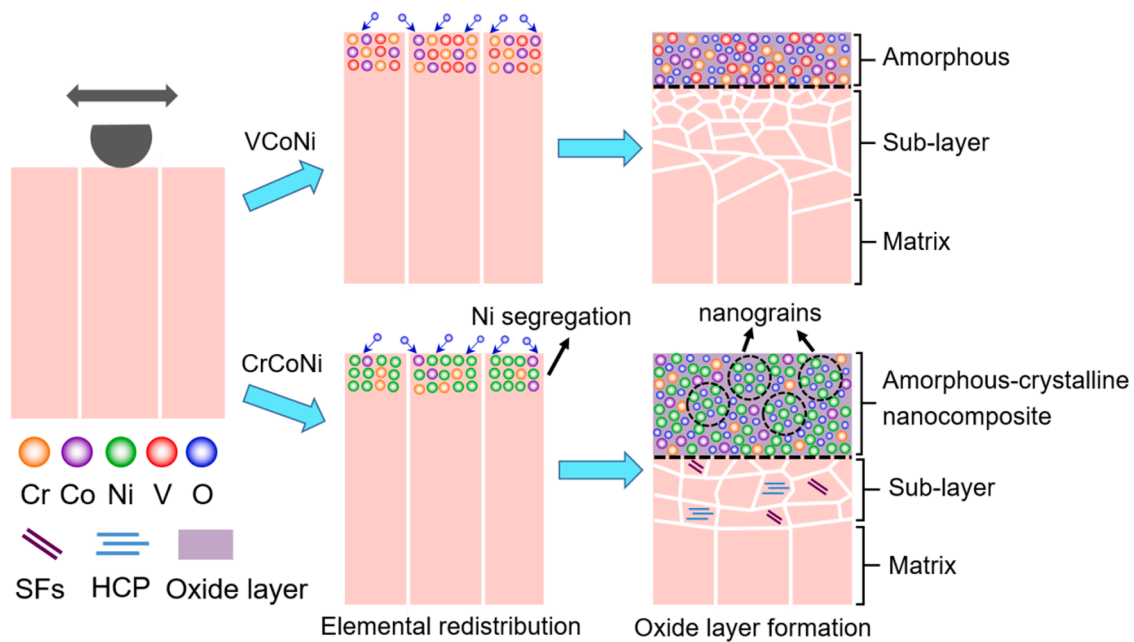
Fig. 13. Schematic of microstructural and chemical evolution for MPEA films.

expected that the thickness of the oxide layer on the VCoNi surface with multi-principal elements should be significantly smaller compared to CrCoNi (Fig. 9). This can be attributed to the enrichment of single Ni principle element in the surface layer of CrCoNi. On the other hand, the presence of this Ni-rich surface layer would simplify the complex composition initially featured by CrCoNi, thereby weakening the susceptibility to friction-induced amorphization in CrCoNi when compared with VCoNi. As a result, an amorphous-crystalline composited structure is formed on the surface of CrCoNi. In contrast, the surface of VCoNi with an equiatomic state exhibits complete oxidation and forms a pure amorphous structure. In summary, compared to VCoNi, the surface segregation of nickel in CrCoNi results in the formation of a distinctive protective layer consisting of amorphous-crystalline oxides.

4.3. Effects of oxide nanocomposite on wear-resistance

The significantly enhanced wear resistance of the CrCoNi film is attributed to the in-situ formation of the dense oxide amorphous-crystalline nanocomposite surface layer. It is noted that the hardness played a pivotal role in the improvement of wear resistance of CrCoNi, which should be attributed to the rather large nano-scale planar defects introduced during the unbalanced magnetron sputtering. On the other hand, according to an approximate evaluation (Supplementary materials), it showed that the formation of tribo-oxide layer made a more contribution to the enhancement in antiwear performance of CrCoNi over VCoNi. The plastic deformation of single phase metallic glass is commonly achieved through the activation and motion of shear bands, which propagate rapidly and lead to catastrophic damage [25,26]. Instead, previous studies have revealed that amorphous-crystalline nanocomposite alloys with nanocrystalline embedded in the amorphous matrix show an outstanding combination of high strength and excellent ductility, attributed to the mutually compatible flow behavior between amorphous and crystalline phase [25]. The incorporation of an embedded nanocrystalline phase could effectively impede the propagation of localized shear bands by means of the division and rotation of nanograins [91]. Evidently, the unique amorphous-crystalline structure mitigates friction-induced strain localization, thereby promoting uniform co-deformation and avoiding cracking at the surface, which plays a pivotal role in enhancing wear resistance. It's also noted that the equi-axed morphology and uniform distribution of nanograins within the

amorphous surface is beneficial for a co-deformation, as they prevent micro-cracks commonly observed between phases in a tribo-layer with irregularly shaped and unevenly distributed grains [22]. Finally, the fully amorphous layer with a thickness of only 10 nm, instead of a nano-composited structure, fails to effectively accommodate the wear-induced plastic deformation in the VCoNi film. The lower wear rate in the CrCoNi film compared to the VCoNi film primarily stems from the contribution of the amorphous-crystalline oxide layer in addition to the film hardness. It can be seen that during frictional deformation, the oxide layer plays a more significant role in enhancing wear resistance by accommodating most of the wear-induced plastic deformation, resulting in a thinner deformed sub-layer. The observed difference in the thickness of the deformed sub-layer between the CrCoNi film (~15 nm) and the VCoNi film (~70 nm) further supports this conclusion. Therefore, the VCoNi film exhibits a thicker deformed sub-layer (~70 nm) primarily due to its thinner oxide layer (~10 nm), which provides less protection against wear-induced stresses. Additionally, the intrinsic hardness of VCoNi is lower than that of CrCoNi, making it less resistant to plastic deformation under the same wear conditions.

5. Conclusions

In summary, the dry wear behavior of ternary MPEAs with mono-phase and nano-grains has been investigated at room temperature. The wear resistance of CrCoNi exceeds that of VCoNi by more than two times. This can be attributed to the occurrence of Ni segregation on the surface. This friction-induced surface segregation is closely related to the weak Cr-Ni bonding, where Ni tends to redistribute towards the surface, reducing the overall potential energy of the system. This Ni-rich surface then undergoes preferential oxidation upon sliding, resulting in the formation of a unique amorphous-crystalline nanocomposite oxide layer. Wear on VCoNi, however, exclusively results in the formation of a thin amorphous layer (Fig. 13). The in-situ-formed amorphous-crystalline nanocomposite layer during wear promotes uniform plastic flow, thereby significantly enhancing the wear resistance of the CrCoNi film. The present study offers a guideline for alloy design in MPEA films to effectively control the formation of nanocomposite oxide layers during friction for excellent wear-resistance.

CRediT authorship contribution statement

Qing Zhou: Writing – original draft, Methodology, Investigation, Data curation. **Zhichao Jiao:** Visualization, Formal analysis, Data curation. **Zhuobin Huang:** Formal analysis, Data curation. **Yeran Shi:** Formal analysis, Data curation. **Yulong Li:** Visualization, Formal analysis, Data curation. **Cunhong Yin:** Formal analysis, Data curation. **Haifeng Wang:** Formal analysis, Data curation. **Haroldo Cavalcanti Pinto:** Writing – review & editing, Visualization, Supervision, Methodology, Funding acquisition, Conceptualization. **Christian Greiner:** Writing – review & editing, Supervision, Project administration, Conceptualization. **Weimin Liu:** Formal analysis, Data curation.

Declaration of interests

The authors declare that they have no known competing financial interests or personal relationships that could have appeared to influence the work reported in this paper.

Acknowledgments

Supplementary materials

Supplementary material associated with this article can be found, in the online version, at doi:10.1016/j.actamat.2024.120299.

References

[1] C. Greiner, J. Gagel, P. Gumbsch, Solids Under Extreme Shear: friction-Mediated Subsurface Structural Transformations, Adv. Mater. 31 (26) (2019) e1806705.

[2] Y. Meng, J. Xu, L. Ma, Z. Jin, B. Prakash, T. Ma, W. Wang, A Review of Advances in Tribology in 2020–2021, 10, 2022, pp. 1443–1595. Friction.

[3] A. Meng, F. Liang, L. Gu, Q. Mao, Y. Zhang, X. Chen, Y. Zhao, An exceptionally wear-resistant CoFeNi2 medium entropy alloy via tribo-induced nanocrystallites with amorphous boundaries, Appl. Surf. Sci. 614 (2023) 156102.

[4] G. Deng, Y. Chong, L. Su, L. Zhan, P. Wei, X. Zhao, L. Zhang, Y. Tian, H. Zhu, N. Tsuji, Mechanisms of remarkable wear reduction and evolutions of subsurface microstructure and nano-mechanical properties during dry sliding of nano-grained Ti6Al4V alloy: a comparative study, Tribol. Int. 169 (2022) 107464.

[5] F. Haftlang, A. Zargaran, S. Son, S. Lee, S.-J. Hong, H.S. Kim, The subsurface deformed region and superficial protective tribo-oxide layer during wear in a non-equiatomic CoCrFeNiV high entropy alloy, Mater. Des. 218 (2022) 110685.

[6] T.J. Rupert, C.A. Schuh, Sliding wear of nanocrystalline Ni–W: structural evolution and the apparent breakdown of Archard scaling, Acta Mater. 58 (12) (2010) 4137–4148.

[7] J. Joseph, N. Haghdadi, M. Annasamy, S. Kada, P.D. Hodgson, M.R. Barnett, D. M. Fabijanic, On the enhanced wear resistance of CoCrFeMnNi high entropy alloy at intermediate temperature, Scr. Mater. 186 (2020) 230–235.

[8] Z. Cheng, L. Yang, Z. Huang, T. Wan, M. Zhu, F. Ren, Achieving low wear in a μ-phase reinforced high-entropy alloy and associated subsurface microstructure evolution, Wear. 474 (2021) 203755.

[9] C.-h. Yin, Y.-l. Liang, Y. Liang, W. Li, M. Yang, Formation of a self-lubricating layer by oxidation and solid-state amorphization of nano-lamellar microstructures during dry sliding wear tests, Acta Mater. 166 (2019) 208–220.

[10] Z. Li, K.G. Pradeep, Y. Deng, D. Raabe, C.C. Tasan, Metastable high-entropy dual-phase alloys overcome the strength-ductility trade-off, Nature 534 (7606) (2016) 227–230.

[11] W. Li, D. Xie, D. Li, Y. Zhang, Y. Gao, P.K. Liaw, Mechanical behavior of high-entropy alloys, Prog. Mater. Sci. 118 (2021) 100777.

[12] D. Hua, X. Liu, W. Wang, Q. Zhou, Q. Xia, S. Li, J. Shi, H. Wang, Formation mechanism of hierarchical twins in the CoCrNi medium entropy alloy, J. Mater. Sci. Technol. 140 (2023) 19–32.

[13] Y.X. Ye, C.Z. Liu, H. Wang, T.G. Nieh, Friction and wear behavior of a single-phase equiatomic TiZrHfNb high-entropy alloy studied using a nanoscratch technique, Acta Mater. 147 (2018) 78–89.

[14] J. Rackwitz, Q. Yu, Y. Yang, G. Laplanche, E.P. George, A.M. Minor, R.O. Ritchie, Effects of cryogenic temperature and grain size on fatigue-crack propagation in the medium-entropy CrCoNi alloy, Acta Mater. 200 (2020) 351–365.

[15] R. Chang, W. Fang, J. Yan, H. Yu, X. Bai, J. Li, S. Wang, S. Zheng, F. Yin, Microstructure and mechanical properties of CoCrNi-Mo medium entropy alloys: experiments and first-principle calculations, J. Mater. Sci. Technol. 62 (2021) 25–33.

[16] W. Ye, M. Xie, Z. Huang, H. Wang, Q. Zhou, L. Wang, B. Chen, H. Wang, W. Liu, Microstructure and tribological properties of in-situ carbide/CoCrFeNiMn high entropy alloy composites synthesized by flake powder metallurgy, Tribol. Int. 181 (2023) 108295.

[17] S. Yoshida, T. Bhattacharjee, Y. Bai, N. Tsuji, Friction stress and Hall-Petch relationship in CoCrNi equi-atomic medium entropy alloy processed by severe plastic deformation and subsequent annealing, Scr. Mater. 134 (2017) 33–36.

[18] J. Li, Y. Huang, X. Meng, Y. Xie, A Review on High Entropy Alloys Coatings: fabrication Processes and Property Assessment, Adv. Eng. Mater. 21 (8) (2019) 1900343.

[19] Y. Zou, H. Ma, R. Spolenak, Ultrastrong ductile and stable high-entropy alloys at small scales, Nat. Commun. 6 (2015) 7748.

[20] S. Alvi, D.M. Jarzabek, M.G. Kohan, D. Hedman, P. Jenczyk, M.M. Natile, A. Vomiero, F. Akhtar, Synthesis and Mechanical Characterization of a CuMoTaWV High-Entropy Film by Magnetron Sputtering, ACS Appl. Mater. Interfaces 12 (18) (2020) 21070–21079.

[21] J. Wang, S. Kuang, X. Yu, L. Wang, W. Huang, Tribo-mechanical properties of CrNbTiMoZr high-entropy alloy film synthesized by direct current magnetron sputtering, Surf. Coat. Technol. 403 (2020) 126374.

[22] J. Luo, W. Sun, D. Liang, K.C. Chan, X.-S. Yang, F. Ren, Superior wear resistance in a TaMoNb compositionally complex alloy film via in-situ formation of the amorphous-crystalline nanocomposite layer and gradient nanostructure, Acta Mater. 243 (2023) 118503.

[23] F. Liang, A. Meng, Y. Sun, Z. Chen, Z. Jiang, Y. Zhang, Y. Zhang, Y. Zhu, X. Chen, A novel wear-resistant Ni-based superalloy via high Cr-induced subsurface nanotwins and heterogeneous composite glaze layer at elevated temperatures, Tribol. Int. 183 (2023) 108383.

[24] X. Liu, J. Fan, J. Pu, Z. Lu, Insight into the high-temperature tribological mechanism of VAlTiCrW high entropy alloy film: alV3O9 from tribochemistry, Friction 11 (7) (2022) 1165–1176.

[25] G. Wu, S. Balachandran, B. Gault, W. Xia, C. Liu, Z. Rao, Y. Wei, S. Liu, J. Lu, M. Herbig, W. Lu, G. Dehm, Z. Li, D. Raabe, Crystal-Glass High-Entropy Nanocomposites with Near Theoretical Compressive Strength and Large Deformability, Adv. Mater. 32 (34) (2020) e2002619.

[26] C. Liu, Z. Li, W. Lu, Y. Bao, W. Xia, X. Wu, H. Zhao, B. Gault, C. Liu, M. Herbig, A. Fischer, G. Dehm, G. Wu, D. Raabe, Reactive wear protection through strong and deformable oxide nanocomposite surfaces, Nat. Commun. 12 (1) (2021) 5518.

[27] D. Jiang, Z. Li, J. Xu, Q. Ren, S.-O. Agbedor, Q. Lei, High-temperature oxidation behaviors of an equiatomic CrMnFeCoNi high entropy alloy, Mater. Today Commun. 32 (2022) 104185.

[28] L. Yang, C. Wei, D. Liang, F. Jiang, Z. Cheng, J. Luan, Z. Jiao, F. Ren, Microstructure evolution and deformation mechanism of coherent L12-strengthened high-entropy alloy during sliding wear, Compos. Pt. B-Eng. 256 (2023) 110651.

[29] S.S. Sohn, A. Kwiatkowski da Silva, Y. Ikeda, F. Kormann, W. Lu, W.S. Choi, B. Gault, D. Ponge, J. Neugebauer, D. Raabe, Ultrastrong Medium-Entropy Single-Phase Alloys Designed via Severe Lattice Distortion, Adv. Mater. 31 (8) (2019) e1807142.

[30] W.-M. Choi, Y.H. Jo, S.S. Sohn, S. Lee, B.-J. Lee, Understanding the physical metallurgy of the CoCrFeMnNi high-entropy alloy: an atomistic simulation study, npj Comput. Mater. 4 (1) (2018) 1.

[31] T. Liang, M. Zhou, P. Zhang, P. Yuan, D. Yang, Multilayer in-plane graphene/hexagonal boron nitride heterostructures: insights into the interfacial thermal transport properties, Int. J. Heat Mass Transf. 151 (2020) 119395.

[32] W. Wang, D. Hua, Q. Zhou, S. Li, S.J. Eder, J. Shi, Z. Wang, H. Wang, W. Liu, Effect of a water film on the material removal behavior of Invar during chemical mechanical polishing, Appl. Surf. Sci. 616 (2023) 156490.

[33] A.K. Rappe, C.J. Casewit, K.S. Colwell, W.A. Goddard III, W.M. Skiff, UFF, a full periodic table force field for molecular mechanics and molecular dynamics simulations, J. Am. Chem. Soc. 114 (1992) 10024–10035.

[34] S. Plimpton, Fast parallel algorithms for short-range molecular dynamics, J. Comput. Phys. 117 (1995) 1–19.

[35] A. Stukowski, Visualization and analysis of atomistic simulation data with OVITO–the Open Visualization Tool, Model. Simul. Mater. Sci. Eng. 18 (1) (2010) 015012.

[36] T.B. Ma, L.F. Wang, Y.Z. Hu, X. Li, H. Wang, A shear localization mechanism for lubricity of amorphous carbon materials, Sci. Rep. 4 (2014) 6.

[37] D.P. Hua, Q.S. Xia, Y.R. Shi, Q. Zhou, S. Li, X.T. Deng, H.F. Wang, Z.D. Wang, Atomistic investigation of the mechanical and tribological responses of the ferrite-cementite interface with a Bagaryatskii orientation, Tribol. Int. 184 (2023) 14.

[38] Y. Ren, Q. Zhou, D.P. Hua, Z.B. Huang, Y.L. Li, Q. Jia, P. Gumbsch, C. Greiner, H. F. Wang, W.M. Liu, Wear-resistant CoCrNi multi-principal element alloy at cryogenic temperature, Sci. Bull. 69 (2) (2024) 227–236.

[39] Y. Chen, D. Chen, X. An, Y. Zhang, Z. Zhou, S. Lu, P. Munroe, S. Zhang, X. Liao, T. Zhu, Z. Xie, Unraveling dual phase transformations in a CrCoNi medium-entropy alloy, Acta Mater. 215 (2021) 117112.

[40] F. Cao, P. Munroe, Z. Zhou, Z. Xie, Medium entropy alloy CoCrNi coatings: enhancing hardness and damage-tolerance through a nanotwinned structuring, Surf. Coat. Technol. 335 (2018) 257–264.

[41] J. Miao, T. Guo, J. Ren, A. Zhang, B. Su, J. Meng, Optimization of mechanical and tribological properties of FCC CrCoNi multi-principal element alloy with Mo addition, Vacuum. 149 (2018) 324–330.

[42] S. Pan, C. Zhao, P. Wei, F. Ren, Sliding wear of CoCrNi medium-entropy alloy at elevated temperatures: wear mechanism transition and subsurface microstructure evolution, Wear. 440-441 (2019) 203108.

[43] J. Joseph, N. Haghdadi, K. Shamlaye, P. Hodgson, M. Barnett, D. Fabijanic, The sliding wear behaviour of CoCrFeMnNi and AlxCoCrFeNi high entropy alloys at elevated temperatures, Wear. 428-429 (2019) 32–44.

[44] A. Ayyagari, C. Barthelemy, B. Gwalani, R. Banerjee, T.W. Scharf, S. Mukherjee, Reciprocating sliding wear behavior of high entropy alloys in dry and marine environments, Mater. Chem. Phys. 210 (2018) 162–169.

[45] L. Yang, Z. Cheng, W. Zhu, C. Zhao, F. Ren, Significant reduction in friction and wear of a high-entropy alloy via the formation of self-organized nanolayered structure, J. Mater. Sci. Technol. 73 (2021) 1–8.

[46] S. Zhu, Y. Yu, B. Zhang, Z. Zhang, X. Yan, Z. Wang, Microstructure and wear behaviour of in-situ TiN-Al2O3 reinforced CoCrFeNiMn high-entropy alloys composite coatings fabricated by plasma cladding, Mater. Lett. 272 (2020) 127870.

[47] Z.X. Wu, M.J. He, C.S. Feng, T.L. Wang, M.Z. Lin, W.B. Liao, Effects of Annealing on the Microstructures and Wear Resistance of CoCrFeNiMn High-Entropy Alloy Coatings, J. Therm. Spray Technol. 31 (4) (2022) 1244–1251.

[48] G. Ma, H. Cui, D. Jiang, H. Chen, X. Hu, G. Zhang, R. Wang, X. Sun, X. Song, The evolution of multi and hierarchical carbides and their collaborative wear-resisting effects in CoCrNi/WC composite coatings via laser cladding, Mater. Today Commun. 30 (2022) 103223.

[49] Z. Zhang, B. Zhang, S. Zhu, X. Tao, H. Tian, Z. Wang, Achieving enhanced wear resistance in CoCrNi medium-entropy alloy co-alloyed with multi-elements, Mater. Lett. 313 (2022) 131650.

[50] Y. Liu, F. Zhang, Z. Huang, Q. Zhou, Y. Ren, Y. Du, H. Wang, Mechanical and dry sliding tribological properties of CoCrNiNb medium-entropy alloys at room temperature, Tribol. Int. 163 (2021) 107160.

[51] K. Xiang, L. Chai, C. Zhang, H. Guan, Y. Wang, Y. Ma, Q. Sun, Y. Li, Investigation of microstructure and wear resistance of laser-clad CoCrNiTi and CrFeNiTi medium-entropy alloy coatings on Ti sheet, Opt. Laser Technol. 145 (2022) 107518.

[52] X. Hao, J. Zhen, X. Zhao, J. Ma, H. Chen, S. Guo, C. Wang, C. Wang, Effect of Sn addition on the tribological behaviors of CoCrFeNi high entropy alloys, J. Alloy. Compd. 909 (2022).

[53] J.-K. Xiao, T.-T. Li, Y.-Q. Wu, J. Chen, C. Zhang, Microstructure and Tribological Properties of Plasma-Sprayed CoCrFeNi-based High-Entropy Alloy Coatings Under Dry and Oil-Lubricated Sliding Conditions, J. Therm. Spray Technol. 30 (4) (2021) 926–936.

[54] A. Silvello, E. Torres Diaz, E. Rúa Ramirez, I. Garcia Cano, Microstructural, Mechanical and Wear Properties of Atmospheric Plasma-Sprayed and High-Velocity Oxy-Fuel AlCoCrFeNi Equiatomic High-Entropy Alloys (HEAs) Coatings, J. Therm. Spray Technol. 32 (2–3) (2023) 425–442.

[55] D. Luo, Q. Zhou, W. Ye, Y. Ren, C. Greiner, Y. He, H. Wang, Design and Characterization of Self-Lubricating Refractory High Entropy Alloy-Based Multilayered Films, ACS Appl. Mater. Interfaces 13 (46) (2021) 55712–55725.

[56] J. Fan, X. Liu, J. Pu, Y. Shi, Anti-friction mechanism of VAlTiCrMo high-entropy alloy coatings through tribo-oxidation inducing layered oxidic surface, Tribol. Int. 171 (2022) 107523.

[57] Y. Wang, N. He, C. Wang, J. Li, W. Guo, Y. Sui, J. Lan, Microstructure and tribological performance of (AlCrWTiMo)N film controlled by substrate temperature, Appl. Surf. Sci. 574 (2022) 151677.

[58] W.H. Kao, Y.L. Su, J.H. Horng, W.C. Wu, Mechanical, tribological, anti-corrosion and anti-glass sticking properties of high-entropy TaNbSiZrCr carbide coatings prepared using radio-frequency magnetron sputtering, Mater. Chem. Phys. 268 (2021) 124741.

[59] N. Tüten, D. Canadinc, A. Motallebzadeh, B. Bal, Microstructure and tribological properties of TiTaHfNbZr high entropy alloy coatings deposited on Ti 6Al4V substrates, Intermetallics. (Barking) 105 (2019) 99–106.

[60] J. Wang, H. Zhang, X. Yu, L. Wang, W. Huang, Z. Lu, Insight into the structure and tribological and corrosion performance of high entropy (CrNbSiTiZr)C films: first-principles and experimental study, Surf. Coat. Technol. 421 (2021) 127468.

[61] B.-S. Lou, F.-R. Kan, W. Diyatmika, J.-W. Lee, Property evaluation of TixZrNbTaFeBy high entropy alloy coatings: effect of Ti and B contents, Surf. Coat. Technol. 434 (2022) 128180.

[62] X. Fan, S. Zheng, S. Ren, J. Pu, K. Chang, Effects of phase transition on tribological properties of amorphous VAlTiCrSi high-entropy alloy film by magnetron sputtering, Mater. Charact. 191 (2022) 112115.

[63] M. Braic, M. Balaceanu, A. Vladescu, C.N. Zoita, V. Braic, Deposition and characterization of multi-principal-element (CuSiTiYZr)C coatings, Appl. Surf. Sci. 284 (2013) 671–678.

[64] S.N. Chen, W.Q. Yan, B. Liao, X.Y. Wu, L. Chen, X. Ouyang, X.P. Ouyang, Effect of temperature on the tribocorrosion and high-temperature tribological behaviour of strong amorphization AlCrNiTiV high entropy alloy film in a multifactor environment, Ceram. Int. 49 (4) (2023) 6880–6890.

[65] X.K. Zeng, Y.T. Li, X.D. Zhang, M. Liu, J.Z. Ye, X.L. Qiu, X. Jiang, Y.X. Leng, Effect of bias voltage on the structure and properties of CuNiTiNbCr dual-phase high entropy alloy films, J. Alloy. Compd. 931 (2023) 167371.

[66] D. Deep Yadav, R. Jha, S. Singh, A. Kumar, Synthesis and characterisation of Nickel oxide nanoparticles using CTAB as capping agent, Mater. Today: Proc. 73 (2023) 333–336.

[67] J. Miao, C.E. Slone, T.M. Smith, C. Niu, H. Bei, M. Ghazisaeidi, G.M. Pharr, M. J. Mills, The evolution of the deformation substructure in a Ni-Co-Cr equiatomic solid solution alloy, Acta Mater. 132 (2017) 35–48.

[68] E.J. Kautz, S.V. Lambeets, D.E. Perea, A.Y. Gerard, J. Han, J.R. Scully, J.E. Saal, D. K. Schreiber, Element redistributions during early stages of oxidation in a Ni38Cr22Fe20Mn10Co10 multi-principal element alloy, Scr. Mater. 194 (2021) 113609.

[69] Z. Zhang, R. Ding, C. Liu, L. Yu, Y. Liu, The precipitates evolution with related element interaction and redistribution during long-term high-temperature aging of Alloy 617, Mater. Charact. 199 (2023) 112783.

[70] D.V. Louzguine-Luzgin, A.S. Trifonov, Y.P. Ivanov, A.K.A. Lu, A.V. Lubenchenko, A.L. Greer, Shear-induced chemical segregation in a Fe-based bulk metallic glass at room temperature, Sci. Rep. 11 (1) (2021) 12.

[71] A. Tamm, A. Aabloo, M. Klintenberg, M. Stocks, A. Caro, Atomic-scale properties of Ni-based FCC ternary, and quaternary alloys, Acta Mater. 99 (2015) 307–312.

[72] X. Chen, Q. Wang, Z. Cheng, M. Zhu, H. Zhou, P. Jiang, L. Zhou, Q. Xue, F. Yuan, J. Zhu, X. Wu, E. Ma, Direct observation of chemical short-range order in a medium-entropy alloy, Nature 592 (7856) (2021) 712–716.

[73] T. Kostiuchenko, A.V. Ruban, J. Neugebauer, A. Shapeev, F. Körmann, Short-range order in face-centered cubic VCoNi alloys, Phys. Rev. Mater. 4 (11) (2020) 113802.

[74] R.K. Nutor, Q. Cao, X. Wang, S. Ding, D. Zhang, J.-Z. Jiang, Accelerated emergence of CoNi-based medium-entropy alloys with emphasis on their mechanical properties, Curr. Opin. Solid State Mat. Sci. 26 (6) (2022) 101032.

[75] R.K. Nutor, T. Xu, X. Wang, X.-D. Wang, P. An, J. Zhang, T. Hu, L. Li, Q. Cao, S. Ding, D. Zhang, J.-Z. Jiang, Liquid helium temperature deformation and local atomic structure of CoNiV medium entropy alloy, Mater. Today Commun. 30 (2022) 103141.

[76] J. Zhang, W. Li, R. Qin, P. Chen, Y. Liu, X. Liu, L. Gao, An atomic insight into the stoichiometry effect on the tribological behaviors of CrCoNi medium-entropy alloy, Appl. Surf. Sci. 593 (2022) 153391.

[77] S. Cheng, M.O. Robbins, Defining Contact at the Atomic Scale, Tribol. Lett. 39 (3) (2010) 329–348.

[78] S. Li, W.T. Ye, Y.R. Shi, Q. Zhou, Y.N. Chen, T. Guo, Y.X. Liu, L.C. Zhang, H. F. Wang, Atomistic simulation and experimental verification of tribological behavior of high entropy alloy/graphene composite coatings, Surf. Coat. Technol. 467 (2023) 129683.

[79] X. Chen, H. Zhong, X. Li, K. Lu, Lowering coefficient of friction in Cu alloys with stable gradient nanostructures, Sci. Adv. 2 (2016) 1601942.

[80] F. Ren, S.N. Arshad, P. Bellon, R.S. Averback, M. Pouryazdan, H. Hahn, Sliding wear-induced chemical nanolayering in Cu–Ag, and its implications for high wear resistance, Acta Mater. 72 (2014) 148–158.

[81] M.P. Agustianingrum, U. Lee, N. Park, High-temperature oxidation behaviour of CoCrNi medium-entropy alloy, Corrosion Sci. 173 (2020) 108755.

[82] W. Wang, D. Hua, D. Luo, Q. Zhou, S. Li, J. Shi, H. Wang, Molecular dynamics simulation of deformation mechanism of CoCrNi medium entropy alloy during nanoscratching, Comput. Mater. Sci. 203 (2022) 111085.

[83] L. Vitos, A.V. Ruban, H.L. Skriver, J. Kollar, The surface energy of metals, Surf. Sci. 411 (1998) 186–202.

[84] S. Zhao, Z. Li, C. Zhu, W. Yang, Z. Zhang, D.E.J. Armstrong, P.S. Grant, R. O. Ritchie, M.A. Meyers, Amorphization in extreme deformation of the CrMnFeCoNi high-entropy alloy, Sci. Adv. 7 (2021) 3108.

[85] H. Wang, D. Chen, X. An, Y. Zhang, S. Sun, Y. Tian, Z. Zhang, A. Wang, J. Liu, M. Song, S.P. Ringer, T. Zhu, X. Liao, Deformation-induced crystalline-to-amorphous phase transformation in a CrMnFeCoNi high-entropy alloy, Sci. Adv. 7 (2021) 3105.

[86] X. Wu, N. Tao, Y. Hong, J. Lu, K. Lu, Localized solid-state amorphization at grain boundaries in a nanocrystalline Al solid solution subjected to surface mechanical attrition, J. Phys. D-Appl. Phys. 38 (22) (2005) 4140–4143.

[87] Y. Ren, Z. Huang, Y. Wang, Q. Zhou, T. Yang, Q. Li, Q. Jia, H. Wang, Friction-induced rapid amorphization in a wear-resistant (CoCrNi)88Mo12 dual-phase medium-entropy alloy at cryogenic temperature, Compos. Pt. B-Eng. 263 (2023) 110833.

[88] B.D. Dawson, S.M. Lee, J. Krim, Tribo-induced melting transition at a sliding asperity contact, Phys. Rev. Lett. 103 (20) (2009) 205502.

[89] A. Takeuchi, A. Inoue, Classification of bulk metallic glasses by atomic size difference, heat of mixing and period of constituent elements and its application to characterization of the main alloying element, Mater. Trans. 12 (46) (2005) 2817–2829.

[90] R. Peraldi, D. Monceau, B. Pieraggi, Correlations between growth kinetics and microstructure for scales formed by high-temperature oxidation of pure nickel. II. growth kinetics, Oxidation Metals 58 (2002) 3.

[91] G. Wu, K.C. Chan, L. Zhu, L. Sun, J. Lu, Dual-phase nanostructuring as a route to high-strength magnesium alloys, Nature 545 (7652) (2017) 80–83.